Spring 2019

Concentration-Dependent Magnetic Properties of MnxNiO1-x Novel Inverted Core-Shell Nanoparticles

Md Nazmul Alam
Missouri State University, Alam39@live.missouristate.edu

CONCENTRATION-DEPENDENT MAGNETIC PROPERTIES OF MN_xNIO_{1-x} NOVEL INVERTED CORE-SHELL NANOPARTICLES

A Master's Thesis

Presented to

The Graduate College of

Missouri State University

In Partial Fulfillment

Of the Requirements for the Degree

Master of Science, Materials Science

By

Md Nazmul Alam

May 2019

CONCENTRATION-DEPENDENT MAGNETIC PROPERTIES OF MN_XNIO_{1-X} NOVEL INVERTED CORE-SHELL NANOPARTICLES

Physics, Astronomy and Materials Science

Missouri State University, May 2019

Master of Science

Md Nazmul Alam

ABSTRACT

The doping concentration (Mn concentration) dependent magnetic properties of NiO@NixMn1-xO novel inverted core-shell magnetic nanoparticles are of great interest of this present research. Primarily, we investigated the oxidation state of Ni from size-dependent four NiO NPs samples, and then studied the variation in the magnetic properties of Mn concentration-dependent NiO@NixMn1-xO CNPs. The NiO nanoparticles were synthesized using a thermal decomposition method. The XRD data indicates that the crystal structure (rock salt) remains fixed in all NiO samples and XPS data shows the oxidation state of size-dependent NiO nanoparticles is 2+. The hydrothermal epitaxy method was used to incorporate Mn in NiO crystal. The resultant product is comprised of antiferromagnetic core (NiO) and ferro/ferrimagnetic shell (NixMn1-xO). The XRD data showed that the crystal structure is identical in both NiO NPs and NiO@NixMn1-xO CNPs and the varying concentrations of Mn have not altered the crystal structure. The XPS analysis indicates the oxidation state of both Mn and Ni is 2+ and the survey scan shows the presence of all constituent elements. The SQUID magnetometer measurements provide us both the ZFC and FC hysteresis loop and indicate the horizontal shift of the FC hysteresis loop in the negative axis of the applied magnetic field which is called exchange bias. The magnetic data shows both the coercivity and the exchange bias of concentration-dependent NiO@NixMn1-xO CNPs are maximum for 0.08 M manganese. The lower resolution TEM image shows most of the CNPs are faceted and some of them are pseudospherical. The HRTEM image gave a clear visualization of the core, shell, and interface region.

KEYWORDS: core-shell nanoparticles, coercivity, exchange bias effect, oxidation state, thermal decomposition, hydrothermal epitaxy

CONCENTRATION-DEPENDENT MAGNETIC PROPERTIES OF MN_xNIO_{1-x} NOVEL INVERTED CORE-SHELL NANOPARTICLES

By

Md Nazmul Alam

A Master's Thesis
Submitted to the Graduate College
Of Missouri State University
In Partial Fulfillment of the Requirements
For the Degree of Master of Science, Materials Science

May 2019

Approved:

Robert A. Mayanovic, Ph.D., Thesis Committee Chair

Kartic C. Ghosh, Ph.D., Committee Member

Tiglet Besara, Ph.D., Committee Member

Julie Masterson, Ph.D., Dean of the Graduate College

ACKNOWLEDGEMENTS

I would like to start with thanking my advisor Dr. Robert A. Mayanovic for helping me with his guidance. I started my MSU life as a novice researcher. I would ask Dr. Mayanovic lots of very simple and illogical questions, but he was very kind to me and remained patient. Honestly, he is the best advisor for beginners. If I had the opportunity, I would select him as my Ph.D. supervisor. I also greatly appreciate the instruction and aid offered by Dr. Kartik Ghosh. He helped me learn how to properly use the SQUID magnetometer and gave me the basic idea about other instruments. Special thanks go to other faculty members for their theoretical and experimental suggestions and to the graduate students of PAMS. Furthermore, I want to mention Dr. Mourad Benamara, the Director of the Institute of Nanoscience and Engineering at the University of Arkansas, Fayetteville, for his help with TEM images and XPS data. Finally, I want to thank to the Department of Physics, Astronomy and Materials Science of Missouri State University for providing enormous facilities to complete my graduate studies here.

I dedicate this thesis to my parents and siblings.

TABLE OF CONTENTS

LIST OF TABLES

LIST OF FIGURES

CHAPTER 1: INTRODUCTION

Due to the strong potential applications, nanomaterials having a size scale less than 100 nm are widely studied in numerous fields; including physics, materials science, chemistry, polymer science, biology, mechanical engineering, pharmaceutical drug manufacture, optical components, cosmetics, and toxicology[1]. Nickel oxide nanoparticles are currently being used in wide-ranging device application, including solid oxide fuel cells, lithium ion microbatteries, electrochromic coatings, catalyst, aerospace, optical filters, automotive rearview mirrors [1]. Some intrinsic properties of NiO, antiferromagnetic nature and high Néel temperature (523 K), make it suitable for room temperature applications, particularly when combined with ferro- or ferrimagnetic phases. One area where NiO nanoparticles have seen considerable application recently is in bimagnetic core-shell nanoparticles (CSNs) [2]–[4]. Bimagnetic CSNs have considerable promise for applications in magnetic devices [4], such as magnetic spin valves, spintronics, and magnetic random-access memory (RAM), as well as for medical applications, including the treatment of hyperthermia, for MRI imaging, and for drug delivery [2], [3].

Small sized nanoparticles are different than the bulk materials due to their novel physical and chemical properties [5]. The surface properties and oxidation state of nanoparticles are controlled by the synthesis environment and the synthesis method. Because nanoscale nickel oxide nanoparticles have diverse and promising applications in various research fields, a number of research groups have been using different techniques in order to alter their surface properties. Although it is not trivial to obtain specifically targeted size and shape (i.e., morphological features) of nanoparticles, this can be accomplished by applying various synthesis techniques such as sol-gel, surfactant-mediated synthesis, thermal decomposition, polymer matrix assisted

synthesis, evaporation, electrodeposition, and spray-pyrolysis [5], [6]. Due to certain advantages, such as low cost, simplicity, high probability of getting pure products, the thermal decomposition method is a widely used method at the industrial level [6]. In our group, we have been successfully using this powerful synthesis technique to grow NiO nanoparticles for couple of years. The most significant parameters of a thermal decomposition system are the decomposition time and temperature to influence the size of nanoparticles. The shape of the nanoscale size particles relies on the pH level of the solution because protonation and deprotonation process effect the surface of the NPs.

Peck et al. [7] reported that the crystalline shape and size strongly influences the physical and chemical properties of nanoscale materials. The number of the surface atoms in proportion to the volume is larger on a nanoparticle (NP) surface in comparison with that of bulk materials. Because of the nature of the electronic structure of nanomaterials, they exhibit very unique chemical and physical properties [8]. Therefore, it can be said that the electronic behavior varies if the size of the particles is modified from less than 10 nm, to comparatively bigger nanoparticles nearing 100 nm. As the size is increased, the surface area of a single NP also gets bigger. Therefore, the probability of having oxidation and hydroxylation on the surface also increases and the different types of defects, such as point defects and oxygen vacancies increases with the NPs size.

As the first chapter of this thesis is mostly related to the X-ray photoelectron spectroscopy (XPS) data analysis, it is necessary to discuss the basic principles of this technique. X-ray photoelectric spectroscopy (XPS) is an exceptionally good surface sensitive quantitative spectroscopic technique to measure elemental composition, chemical state and electronic state of the materials. Figure 1.1 is the schematic diagram of X-ray photoelectron spectroscopy (XPS). In

XPS, a suitable X-ray (e.g., Al Kα) source irradiates the material at very low vacuum pressure (P~10^-8 millibar). The detector simultaneously measures the kinetic energy and the number of electrons coming from the sample material. Since the energy of the source, such as Al Kα, is known and the kinetic energy of each electron is measured by the detector, the binding energy of each of the electron can be calculated by using the equation: $E_{binding} = E_{photon} - (E_{kinetic} + \Phi)$

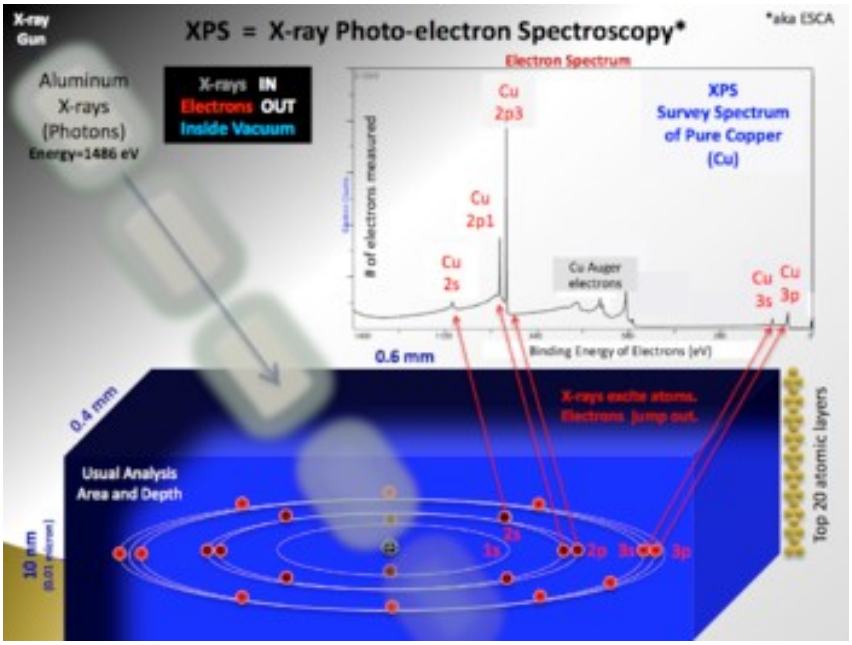

Figure 1.1: Rough schematic of XPS basic principal[9]

Here $E_{binding}$ is the binding energy of each of the electron, E_{photon} is the energy of the source, $E_{kinetic}$ is the kinetic energy of each of the emitted electron and Φ is the work function of the material, which is an intrinsic property of its surface. Since the sampling depth of XPS is about 10 nm, this system can successfully be used to analyze the surface quality of differently sized nanomaterials ranging from few nanometers to bulk materials. The characteristics spectra are reflective of the different elements contained within each sample where each of the XPS peaks, such as the Ni 2p, O 1s, etc. contain the quantitative and surface chemical information

pertinent to the sample. It has to be kept in mind that not all of the emitted electrons can reach to the detector because of inelastic collisions, recombination, excitation of the sample, trapping or recapture by the other energy states of the sample[9]. Nevertheless, this can be calibrated for by proper standardization techniques.

The XPS process is as follows. The emitted photoelectron from the electronic core level creates an excited ion with excess energy which is relaxed by an outer level electron. The relaxation of the excited ion either produces an X-ray or another electron, called the auger electron, is ejected from the valance band and reaches the detector (Figure 1.2). The auger electron contributes to create features in the spectra called auger peaks. The transition metals can generate shake-up peaks at higher binding energy than the main peak, because of reduced energy of the photoelectron by the interaction with the relaxing electron.

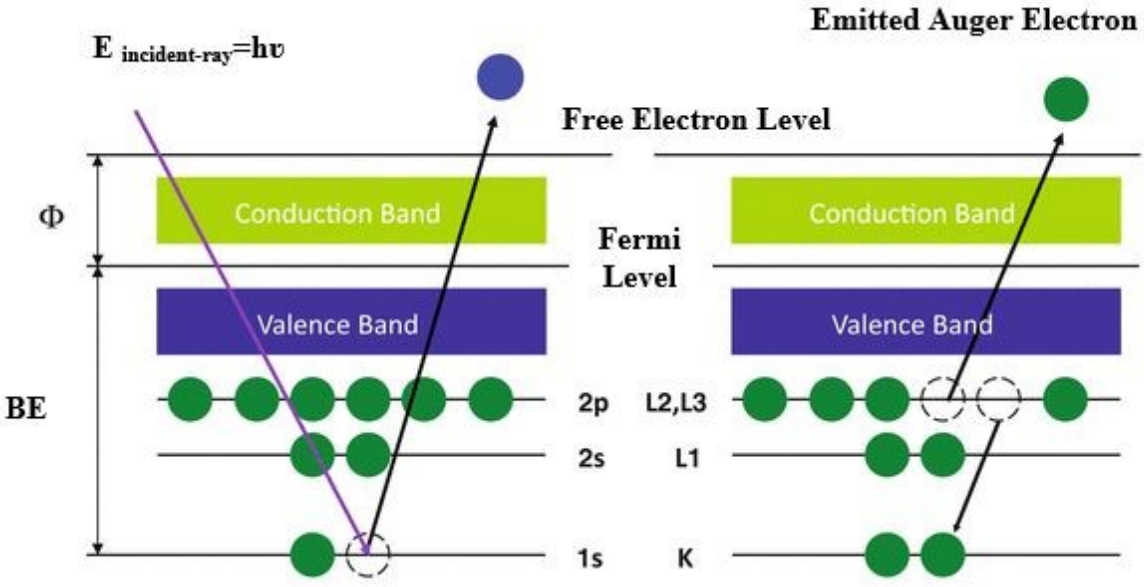

Figure 1.2: Photoelectron and auger emission process[10].

In some cases, the excited ion becomes relaxed by losing an electron from the lower energy state: this electron will be presented in the survey spectra as a shake-off peak[11], [12]. Generally, the XPS technique can provide spectra for all the elements except those having an atomic number (Z) less than three. Each element within the sample produces individual XPS characteristic peaks at specific binding energies [9]. Apart from the primary photoemission peaks for each element, an XPS survey spectrum shows the corresponding auger peak and high resolution spectra often show additional peaks, including satellite peaks, shoulder peaks, shake-up peaks. In this present manuscript, shoulder peak and main peak broadening and position of satellite peak play a significant role in distinguishing feature of different sized nanoparticles.

Previous investigations reported that the nano-size of particles impacts the near-surface electronic structure, while others disagreed with this conclusion. In the study of bulk vs nanosized NiO particles, Bijou and Kadar[8] concluded that the Ni 2p and the satellite peak are directly reflective of Ni 3d-O 2p hybridization, surface defects, and local and non-local screening. On the other hand Peck et.al.[7]argued that the mainline shape and satellite structure can be varied because of the size of NiO nanoparticles, their surface to volume ratio, and Ni^{2+} ion vacancies on the surface of the NPs[8]. These researchers have shown that the peak position does not change with the size of the NPs [7] and is simply due to the persistent Ni^{2+} oxidation state. Because of the local and non-local screening, a shoulder peak might appear on the high energy side of the Ni2p3/2 and Ni2p1/2 main peak [7], [8]. The surface properties of nanoparticles play a key role in determining the characteristics (elemental composition, oxidation state) of NPs and increasing their size may increase the number of NiO_6 clusters on the surface. The possible local and non-local screening might be more pronounced in larger particles and lower in smaller particles as the number of NiO_6 units is reduced with size of the NPs. The above

discussion illustrates how the nanoscale size impacts the near-surface electronic structure as exhibited in XPS spectra.

Furthermore, it has been verified that hydroxylation of the surface of NiO nanoparticles also depends on the size of the nanomaterials. The thermal decomposing synthesis technique is a direct chemical process using water as a solvent. In addition, it has also been shown that water molecule can be present on the surface of nanomaterials [8]. Recently, in our group a series of NiO nanoparticles have been synthesized, ranging in size from 8.3 nm to 47.6 nm. The characterization of these nanoparticles has been made using X-ray diffraction (XRD) and X-ray photoelectron spectroscopy (XPS). The raw data from XRD is analyzed using TOPAS software and the XPS data is fitted using CasaXPS software.

The third chapter of this thesis mostly will provide an introduction to inverted magnetic core shell nanoparticles (CSNs). In nanotechnology, hydrothermal synthesis is playing a significant role in the preparation of nanomaterials for the advancement of the nanodevice fabrication. The hydrothermal process involves a heterogeneous reaction, in which the aqueous solution is kept under high pressure and temperature [3], [13], [14]. The very third chapter of this dissertation will discuss magnetic properties, namely the hysteresis and exchange bias properties of the magnetic core-shell nanoparticles (CSNs). Our research group actively has been using the hydrothermal process for the preparation of inverted magnetic core-shell nanoparticles. Research involving nanomaterials is very important because of the considerable potential for providing solutions to outstanding issues in various fields, such as electronics, energy conversion, medical technology, biomedical engineering, space technology, information and communication technology, and computation. The modified dimensions of the nanomaterials can provide distinctive properties, including optical, magnetic, mechanic, thermal, and electric properties. For

magnetic applications, these properties can be applicable to magnetic random excess memory, spintronics device, quantum computing, hyperthermia, MRI imaging, drug delivery, spin valves, and other areas [3], [15]–[17]. The combination of ferromagnetic/ferrimagnetic (FM/FiM) and antiferromagnetic (AFM) property in NPs make these potentially favorable for applications due to the interaction between the FM/FiM and AFM component through the exchange bias effect.

Core-shell nanoparticles (CSNs) are an excellent example of multicomponent NPs with core, shell and the coupling interface region being relevant to their performance. Figure 1.3 is the diagram of the conventional core-shell nanoparticles. Bimagnetic core-shell nanoparticles are typically synthesized by incorporating 3d transition metals (e.g., Ni, Co, Fe, etc.) using various synthesis techniques. The magnetic properties of such CSNs are found to depend on the nature and quantity of 3d metal(s) and typically involve formation of a metal oxide component. Hu found that Co-doped NPs exhibit an increase in hysteresis loop area and coercivity, whereas Ni-doped nanoparticles showed a reduction in these magnetic characteristics [18].

Normal magnetic core shell nanoparticles are made of an FM/FiM core and an AFM thin shell, marked with an interface between them. Ones having an AFM core and FM/FiM shell are called inverted core-shell nanoparticles. In this thesis, I discuss my study of inverted CSNs having an AFM NiO core and an FM/FiM $Mn_xNi_{1-x}O$ shell. The interface is critical for providing the mechanism of interaction between core and shell in bimagnetic CSNs. The interaction between the AFM core and FM/FiM shell is termed the exchange bias effect (EB). The exchange bias phenomenon has been studied intensively over the past forty years or so. The initial development of the EB effect was made by Meiklejohn and Bean in 1956 [19] and then Jacobs and Bean in 1966 [19]. The EB effect is typically manifested by a shift of the field cooled (FC) hysteresis loop along the horizontal (field) axis with respect to the zero field cooled (ZFC)

hysteresis loop [20], [21]. In addition, a vertical shift of the FC vs ZFC hysteresis loop has been attributed to the EB effect [21]. The EB effect is actuated by the interaction of the magnetic spins at the AFM/FM or AFM/FiM interface.

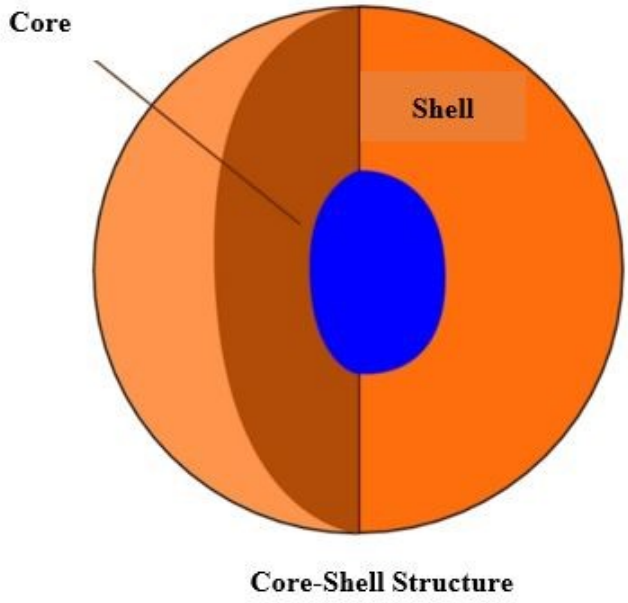

Figure 1.3: Schematic of core shell nanoparticle [22].

The exchange bias in thin films has significant potential for and ongoing application in device fabrication because of the relative ease of control of the EB effect. Nevertheless, the basic principles of the exchange bias spin-spin coupling is still not entirely understood [23]. Researchers have developed a variety of synthesis methods and lithographic techniques to fabricate well-controlled nanoscale materials, in order to shed more light on the EB effect at the nano-level. As stated above, the FM-AFM interface may produce an exchange bias effect that is manifested in many ways, such as in a horizontal shift, vertical shift, an enlargement or distortion of the FC hysteresis loop with respect to the ZFC hysteresis loop.

Figure 1.4 shows the schematic diagram of the exchange bias mechanism. It is evident from the diagram that FC hysteresis loop shift happens in five distinctive steps. Above the Neel temperature (T_N), antiferromagnetic spins are randomly oriented because the antiferromagnetic materials manifest weak magnetism. On the other hand, ferromagnetic spins are parallel with one another below Curie temperature (Tc). As Tc is greater that T_N, as the temperature is cooled below T_N the AFM spins align in a parallel arrangement with the FM spins. The second step of Figure 1.4 shows that FM spins are firmly coupled with AFM spins at the interface. This coupling interaction provides an additional force to the FM spins. For that reason, an external magnetic force is needed to break down the coupling AFM-FM spin coupling: A large magnetic anisotropy of AFM spins requires a large external magnetic force and shifts the hysteresis loop along the horizontal axis whereas a weak AFM anisotropy enhances the coercivity of the system [24]. Depending on the synthesis process, doping concentration, morphology, and other factors, the CSNs may have point defects, line defects, ion or oxygen vacancy in the core-shell interface, which in turn affect their EB and other magnetic properties. This anisotropy of AFM spins is similar for nanoparticles and thin films. Steps 2 and 3 of Figure 1.4 show the coupling of AFM spins with the FM spins for an FC hysteresis loop measurement. The external magnetic field applied in the reverse direction tries to switch the spin orientation of FM region whereas the AFM spins are much more resistant to change their orientation. As the applied reverse magnetic field grows, the magnetic torque applied to the FM spins becomes sufficiently large so as to reverse their orientation to the point where the magnetization goes to zero and the hysteresis curve intersects the field or horizontal axis. This intersection point defines the negative coercivity of the FC hysteresis of the material. In step 4, the applied magnetic field is

sufficiently large in the negative direction so as to completely reverse all of the FM spins relative to the starting orientation in step 2.

The pinned AFM spins perform a central role, via the interaction with the uncompensated FM spins at the interface, in causing the negative shift of the FC vs ZFC hysteresis loop along the field axis. As illustrated in step 5 in Figure 1.4, the AFM spins exert an additional torque on the FM spins when the applied magnetic field is applied in the positive direction.

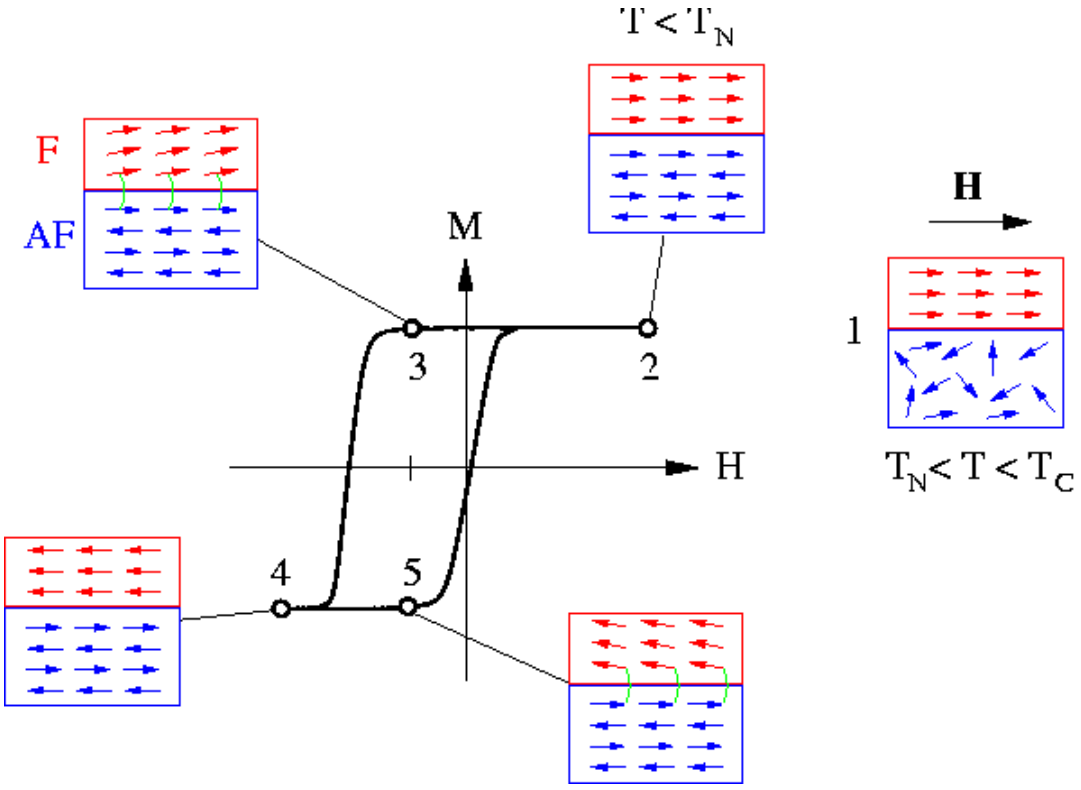

Figure 1.4: The FC hysteresis loop showing the EB effect in a bimagnetic system: The various steps are described in the text [25].

Therefore, less force is needed to flip the FM spins along the positive field axis and the FC hysteresis loop is once again shifted in the negative field axis direction relative to the ZFC loop. The thickness of FM and AFM layers and interface roughness generally control EB of the

thin film, but exchange coupling of NPs depends on doping concentration, size of a particle, the thickness of the shell, the roughness (at the crystalline level) of the interface, and shape of the particles.

In core shell nanoparticles (CSNs), core size and shell thickness have a significant impact on the coercivity and the exchange coupling of the CSNs. Salazar-Alvarez showed that the core size along with the ratio of core diameter to shell thickness have a direct bearing on the exchange coupling and coercivity [26]. Hosain et al. have recently demonstrated that $NiO@M_xNi_{1-x}O$ (M: Mn, Co) inverted core shell nanoparticles can provide substantial coercivity (Hc) values and while also providing an exchange bias field (Heb) [3]. The objective is to find a way to fabricate such CSNs which will have applications at room temperature. The $NiO@Mn_xNi_{1-x}O$ CSNs offer considerable promise for such applications. Another important consideration in magnetic nanostructured materials is the existence of either single or multiple magnetic domains, which is a key variable to determine the so-called superparamagnetic behavior of NPs. As Figure 1.5 shows, for sufficiently small sized NPs, the NP size coincides with the single magnetic domain size and the system is said to be superparamagnetic at sufficiently low temperatures. As the NP size increases, the domain size increases along with it until the size becomes large enough for the formation of multiple domains. Each of the domains has a net magnetic moment derived from the collection of all spins (for ideal FM or FiM configurations) called the magnetic dipole moment. Figure 1.5 shows how the magnetic domain size of the nanoparticles affects the coercivity: the optimum domain size providing the largest coercivity of the nanoparticles occurs just at the point of splitting from single to multiple domains. This occurs because of the overall cancellation of the magnetic dipole moments due to each of the domains becoming more progressive with increasing NP size. Additionally, the outer

layer of NPs may play a role in the magnetization due to uncompensated spins depending upon the so-called surface magnetic anisotropy. Obviously, as the temperature is increased beyond either the Tc or T_N limit, the magnetization of the NPs is diminished due to thermal disorder of the spins.

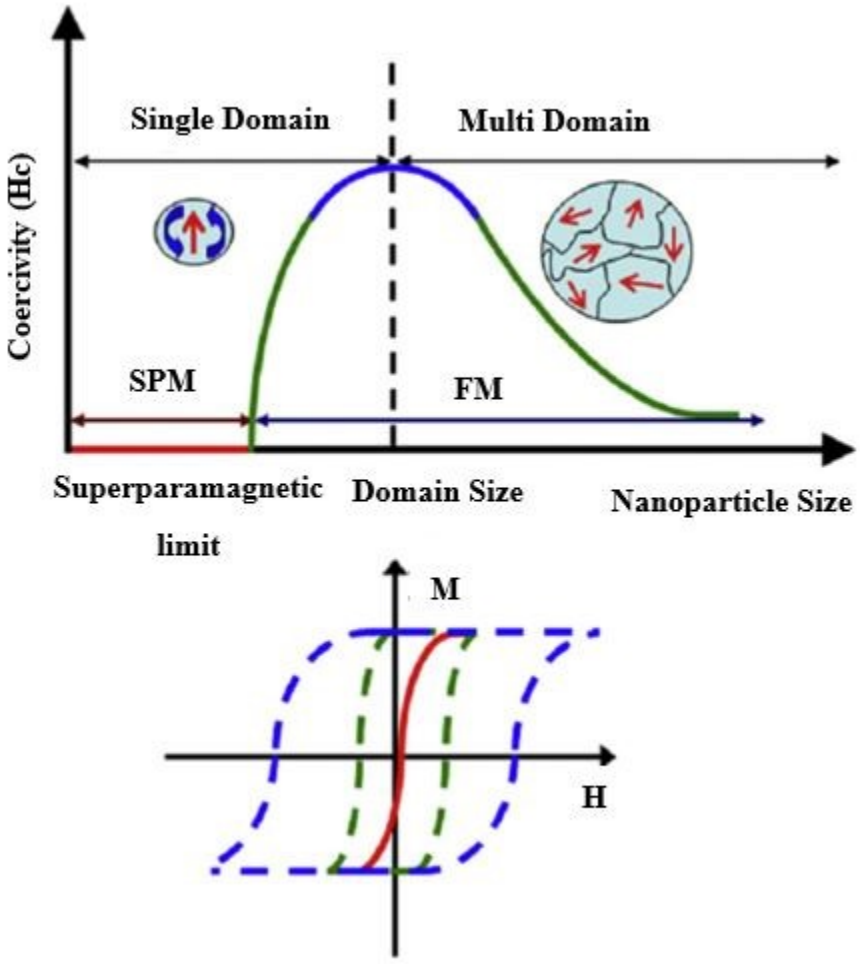

Figure 1.5: The size dependent quantitative behavior of magnetic nanoparticles [27].

The nanoparticle size, or more specifically the core size, may have an effect on the exchange bias of CSNs due to its direct impact on the surface to volume ratio at the location of the core-shell interface. This has been verified in the case of Co (Co@CoO?) and Fe

(Fe@Fe2O3?) passivated oxide CSNs [24], [28], [29] with particles size ranging from 6 - 10 nm. The shell region should have a minimum thickness and the anisotropy energy in the AFM region must be greater than the interfacial energy to observe Heb. The doping concentration can also have a significant impact on the Heb and Hc values of CSNs, particularly in how it affects the properties of either the core or the shell wherein the doping occurs. For my work, the introduction of the 3d transition metal dopant in the shell of CSNs is of interest as this has the potential to change the magnetism from an AFM to FM or FiM type within the compound metal oxide phase. It has been shown that the magnetic behavior of $M_xNi_{1-x}O$ is M concentration dependent. However, excessive incorporation of transitional metal into metal oxide may break down original crystal structure thus adversely affecting the magnetic properties of the material.

In previous studies, researchers concentrated on synthesis of core-shell structured nanoparticles using partial oxidation of metal (i.e., Co, Fe, Ni, etc.) nanoparticles. Some very well-known examples of such CSNs include Ni@NiO, Co@CoN, $Fe@Fe_2O_3$, $CrO_2@Cr_2O_3$, and $Fe_3O_4@FeO$ [24]. These types of CSNs are typically synthesized using a chemical assists or a co-precipitation method and have a single metal element and have an FM or FiM core with an AFM shell. The chemical assists process is well suited for incorporation of more than one transitional metal in the same core-shell (CS) structure. There is very high probability of producing formation of two different phases and for creation of a highly disorder interface, which is an important issue for providing substantial EB in CSNs. On the other hand excessive oxidation may affect the integrity of the core, which may form paramagnetic materials.

In our lab, CSNs FM/FiM shell and AFM core have been grown using the hydrothermal epitaxy method. It is now a widely preferable technique because of its flexibility in getting different morphology, very smooth and well-ordered interface and it does not have any limitation

in metal substitution of different elements within the starting structure of the core. The strength of exchange coupling between core and shell is determined by the crystalline nature of the interface. This method gives us an opportunity to get bimagnetic novel inverted core shell CSNs in replacing conventional CSNs. In my project, I worked on inverted magnetic NiO@$Ni_xMn_{1-x}O$ CSNs and studied the oxidation state of NiO nanoparticles. The crystal structure was measured using X-ray diffraction (XRD) method and the XRD data were analyzed using the TOPAS software. The atomic concentration and oxidation state of different elements have been calculated using X-ray photoelectron spectroscopy (XPS) and the raw data have been fitted using CasaXPS software. The transmission electronic microscopy (TEM) was used to provide imagery of cross sections of single nanoparticles, particle size distributions and corollary structural data. SQUID magnetometry was used to characterize the magnetic behavior of bimagnetic inverted NiO@$Ni_xMn_{1-x}O$ CSNs.

CHAPTER 2: SIZE-DEPENDENT ELECTRONIC PROPERTIES OF NIO NANOPARTICLES AS DEDUCED FROM XPS RESULTS

Abstract

NiO is antiferromagnetic with a high Néel temperature (523 K) making it highly suited for magnetic and spintronic applications. Nickel oxide nanoparticles (NPs) were synthesized using the thermal decomposition method. The size of the NiO NPs was controlled by varying the decomposition time and temperature. The characterization was made using X-ray diffraction (XRD) and X-ray photoelectron spectroscopy (XPS) whereas the data were fitted using TOPAS and CasaXPS software, respectively. The XRD analysis showed that all the NiO samples have similar rock salt crystal structure and that the calculated NP size, as calculated using the Scherrer equation, is in the range from 8.3 nm to 47.3 nm. The X-Ray Photoemission Spectroscopy (XPS) measurements made on the NPs showed that the peak position in the Ni 2p region and O 1s region remained fixed for all the four samples. The position of the Ni 2p1/2, Ni 2p3/2, and their corresponding satellite peaks are always approximately the same for all the size- dependent NiO NPs. A satellite peak occurring at ~1.8 eV on the higher energy side of the Ni 2p3/2 and the O 1s peaks was found to vary intensity with nanoparticle size. The larger particles have a broader satellite peak than the smaller NPs, which is attributed to the variation in surface area. The satellite peak is due to the local and nonlocal screening on the surface of the NiO nanoparticles. Similar broadening of the O 1s peak is attributed to the more prominent impurity peaks, including the hydroxide and H_2O peaks, on the larger NPs.

Introduction

The unique properties of nanoparticles (NPs) separate them from their counterpart bulk materials. Presently, researchers from all over the world are investigating the chemical and physical properties of NPs that are owed to their nanoscale size that bridges the domain between that of atoms and micron sized materials. A number of prominent properties (e.g., catalytic, optoelectronic, etc.) can be attributed to defects on the surface (such as line or point defects, vacancies, etc.), and morphology (i.e., shape and form) of NPs. The surface to volume ratio is another very important parameter in controlling the properties of NPs. Different synthesis techniques, such as sol-gel, surfactant-mediated synthesis, thermal decomposition, poly matrix assisted synthesis, and spray pyrolysis, have allowed scientists to vary the properties of NPs [1]. Transition metal oxide NPs have been gaining attention in a number of fields such as physics, materials science, chemistry, polymer science, biology, mechanical engineering, pharmaceutical drug manufacture, optical components, cosmetics, and toxicology [2].

Nanomaterials with size in the range of a few nanometers to 100 nm are being used as solid oxide fuel cells, lithium ion micro batteries, electrochromic coatings, catalysts, aerospace materials, optical filters, automotive rearview mirrors, battery cathodes, and gas sensors [2], [3]. NiO nanomaterials have recieved attention because of their antiferromagnetic nature and high Néel temperature (523 K). These properties make them suitable for room temperature applications, particularly when combined with ferro- or ferrimagnetic phases. Bi-magnetic core-shell nanoparticles (CSNs) are considered as a high potential research area for antiferromagnetic NiO nanoparticle. Bi-magnetic CSNs have very promising applications in magnetic devices, such as magnetic spin valves, spintronics, and magnetic random-access memory (RAM), as well

as for medical applications, including the treatment of hyperthermia, for MRI imaging, and for drug delivery [2], [4]–[6].

Previous investigations of how the nanoscale size impacts the near-surface electronic structure of NiO NPs as exhibited in XPS spectra show contradictory results. Biju and Khadar [7] concluded that the considerably larger surface-to-volume ratio controls the broadening of the Ni 2p3/2 peak and its corresponding satellite peak. They reported that the satellite peak position, occurring at ~1.5eV higher binding energy side of the 2p 3/2 main line peak, remains almost constant for both bulk and nanoparticles. However, these authors only made XPS measurements of NiO NPs of one size only. Prior research has purported that local screening effects, arising from the Ni 3d-O 2p hybridization at NiO_6 units, and non-local screening effects, occurring due between different NiO_6 units within larger NiO clusters, are responsible for the XPS satellite features [7], [8]. Biju and Khadar [7] speculated that the larger surface area (in relation to the volume) of NiO NPs should have a considerably greater number of terminal NiO6 units than bulk NiO. Therefore, the non-local screening should be more enhanced in smaller NPs (due to the larger surface-to-volume ratio) and less enhanced in larger NiO nanoparticles. My study involves a systematic examination of the XPS spectra measured from an array of NiO NPs with size ranging from 8.3 to 47 nm, in order to test the hypothesis put forward by Biju and Khadar [7] concerning the broadening of the Ni 2p3/2 peak and associated features. The characterization of the NiO nanoparticles was made using XRD and XPS techniques. X-ray diffraction was used to measure the crystal structure and nanoparticle size and X-ray photoelectron spectroscopy (XPS) analysis was used to determine the oxidation state of Ni and its bonding environment in the NiO NPs.

Experimental Methods

The NiO nanoparticles (NPs) were grown using the thermal decomposition method which is an effective technique to tune various sized and shaped NPs. In the past, people have used this synthesis process to produce NiO nanoparticles. The following flow chart (figure 2.1) of thermal decomposition gives a very clear idea of the steps and process. It is evident from the flow chart that the synthesis process takes several steps to grow NiO nanoparticles. The thermal decomposition synthesis method was directly followed from the description given by El-Kemary et. al [3]. Our lab has been following this technique for producing nickel oxide nanoparticles for a number of years. According to El-Kemary et. al [3], the necessary chemicals are nickel chloride hexahydride (NiCl2.6H2O), hydrazine monohydrate solution, and NaOH or KOH. The description of the thermal decomposition method can be followed from the flow chart in Figure 2.1. At the very first step of synthesis, nickel chloride hexahydrate (0.11) was added to alcohol to make a solution. Thereafter, the solution had been sonicated and then hydrazine monohydrate was added to the solution according to the chemical reaction equation. The pH level of the solution was adjusted to 8 by adding NaOH to the solution. Although, Hasan et. al.[5] and Kemary et.al. described that the solution needed to be stirred for 2 hours at room temperature, less than two hours stirring can produce a pure precursor. After that step, the solution was kept for 2 hours or more to get the precipitate the sample and then the sample was washed by using DI water and centrifuged 4-5 times to remove all impurities. The resultant product, Ni(OH)2 .0.5H2O, was then kept inside a box at 50˚C to dry it.

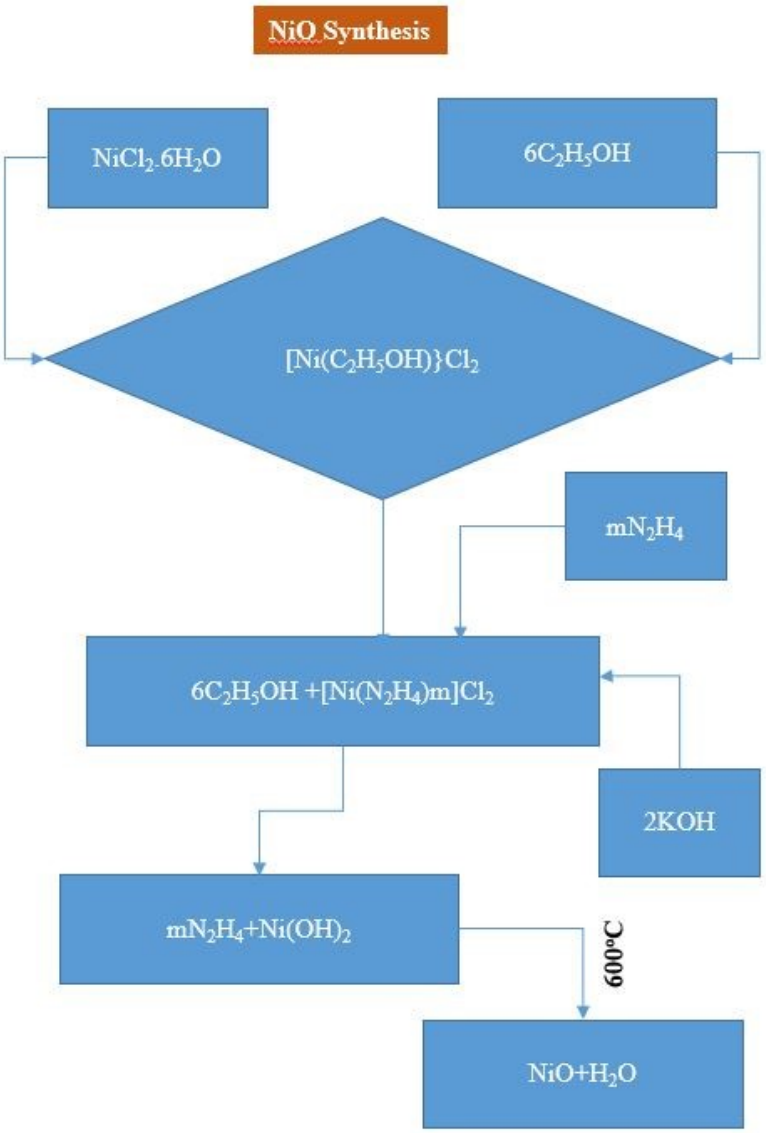

Figure 2.1: Flow chart of thermal decomposition process.

The different steps of the flowchart are executed by the following chemical reactions:

$$NiCl_2.6H_2O + 6C_2H_5OH = [\ Ni(C_2H_5OH)_6Cl_2$$

$$[Ni(C_2H_5OH)_6Cl_2 + mN_2H_4 = 6C_2H_5OH + [Ni(N_2H_4)m]Cl_2$$

$$[Ni(N_2H_4)m]Cl_2 + NaOH = mN_2H_4 + Ni(OH)_2$$

$$Ni(OH)_2 = NiO + H_2O\ (600^oC)$$

Some research groups, however, reported that the chemical reactions produced Ni(OH) as the resultant product [3], [5], but my XRD measurements, made at this step of the synthesis process, verified that the final outcome was metal Ni nanoparticles. Nickel nanoparticles were then heated inside a furnace in an oxygen environment for thermal decomposition. The maximum decomposition temperature was 600˚C but the decomposition time was varied from 1 hours to 2 hours. I have grown different-sized NiO nanoparticles ranging from 8.3 nm to 47.3 nm in diameter. Some parameters of synthesis control the size and morphology of NiO NPs. The thermal decomposition time and temperature may alter the size of NiO nanoparticles.

The TEM imaging was made using the Cryo-Transmission Electron Microscope facility at the University of Arkansas. The crystal structure of the NiO nanomaterials, measured by X-ray photoelectron diffraction, was made using Brucker D8 Discover at Missouri State University. The operating voltage and current were 40kv and 40 amp respectively and CuKα source produced X-ray with λ=1.54184 Å wavelength . TOPAS software had been used to calculate the diameter of NiO using Scherrer equation. The XPS data were measured using the PHI Versaprobe XPS scanning X-ray monochromator facility from the University of Arkansas. CasaXPS software was used to process and fit the raw XPS data.

Results and Discussion

Figure 2.2 shows the powder X-ray diffraction pattern of four different NiO nanoparticles with various particle size. The measurement were made at room temperature for all of the NiO NP samples. The figure indicates that the XRD data, which are indicative of the rock-salt structure, are consistent for all of the NiO NP samples. The XRD data are devoid of impurity peaks indicating the purity of the NiO NPs.

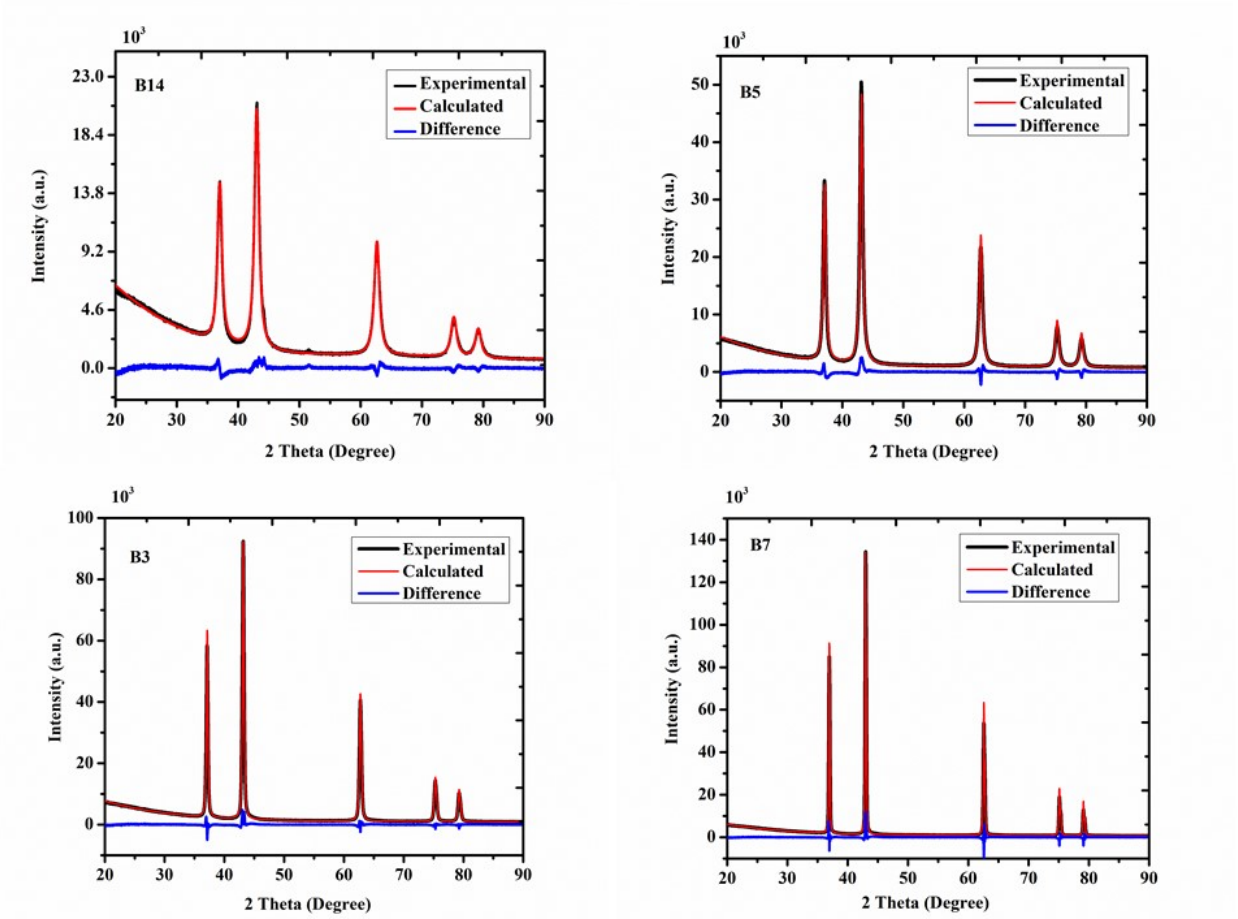

Figure 2.2: X-ray diffraction patterns for the different sized NiO nanoparticle samples: top left: B14; 8.3 nm, top right: B5; 15.67 nm, bottom left B3; 27.6 nm, bottom right: B7; 47.3 nm.

TOPAS software was used to analyze the XRD data, from which it was confirmed that the NiO NP samples have the rock-salt crystal structure with space group Fm-3m. The crystalline size of the NiO nanoparticles was determined using the Scherer formula. It is found that the size of B14, B5, B3 and, B7 samples is 8.3 nm, 15.6nm, 27.6 nm, and 47.3nm, respectively. Figure 2.2 shows a greater peak broadening with decreasing size of the NP samples. As Table 2.1 shows, the FWHM of the NiO (200) peak is strongly affected by the size of the NiO NPs.

Table 2.1: Peak position and FWHM of the NiO (200) peak for the NiO NP samples.

Batch	Size of the NiO NPs(nm)	Peak position(2θ)	FWHM
B7	47.60	43.00	1.45
B3	27.60	43.18	2.46
B5	15.67	43.08	3.97
B14	8.27	43.06	8.34

Table 2.1 shows that the (200) peak position remains consistent for the NiO NP samples, which is an indication that the oxidation of the Ni^{2+} ion is fixed. In addition, the FWHM data in the above table manifests peak broadening for lower sized nanoparticles. Figure 2.3 shows a typical XPS survey spectrum measured from the nickel oxide nanoparticles. The survey spectrum shows the Ni2p, Ni3s, Ni3p,O1s and the Ni auger peak features. The intensity of the Ni 3s and Ni 3p peaks is considerably lower in comparison with that of the Ni 2p peak. The elemental composition in a compound is measured by analyses of the highly intense mainline peaks. In the case of NiO nanoparticles, the Ni 2p and O 1s are the higher intensity mainline peaks for Ni and O, respectively. In this research project, XPS analyses were made of the high-resolution Ni 2p and O 1s spectra for all of the NiO NP samples. Figure 2.4 shows the high-resolution Ni 2p specta for the four different samples. All the four figures show that the peaks position for all the Ni 2p 3/2, Ni 2p 1/2, and satellite peaks, have fixed positions from sample to sample. For instance, Ni 2p3/2, Ni2p3/2 sat (main satellite peak), Ni 2p1/2, Ni 2p1/2 sat, and the secondary satellite peak always are at 853.8 eV, 860.6 eV, 872 eV, and 879.2 eV respectively

[8]. Since the binding energy of the mainline peaks has not changed, which is an indication of the oxidation state of the nickel ion, N^{2+}, for all the samples. The spin-orbit coupling splits the 2p orbital into two different subshells, namely the 2p3/2 and 2p1/2. The separation binding energy between two of them in invariably persistent irrespective of the size of the particles

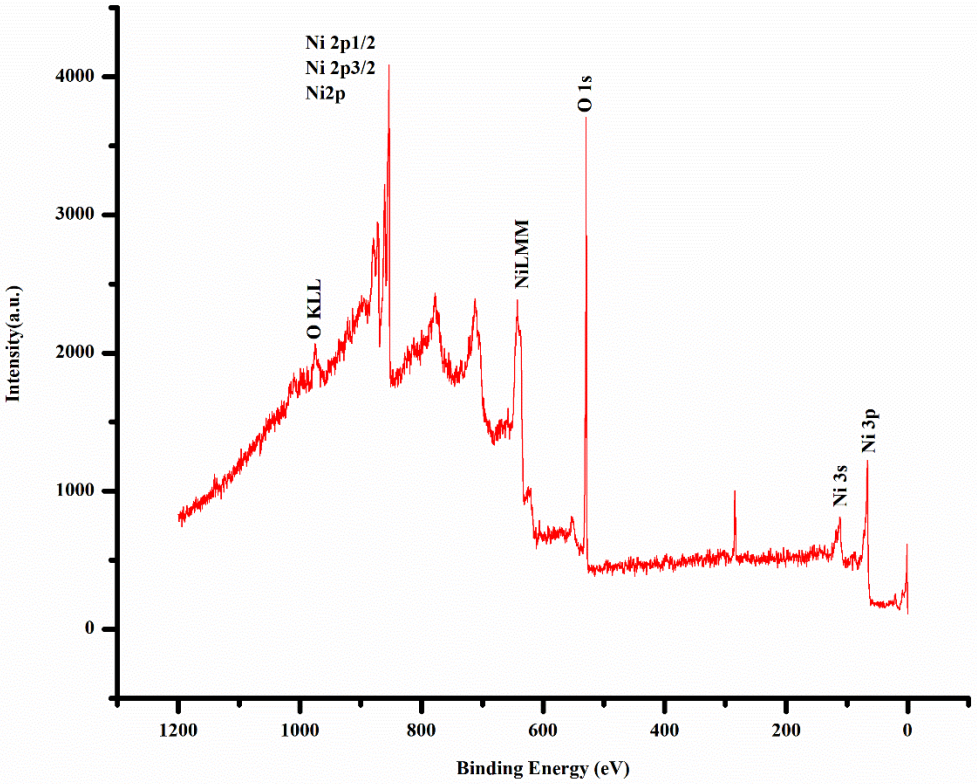

Figure 2.3: XPS survey spectrum of Nickel Oxide nanoparticles.

The separation binding energy between two of them in invariably persistent irrespective of the size of the particles.

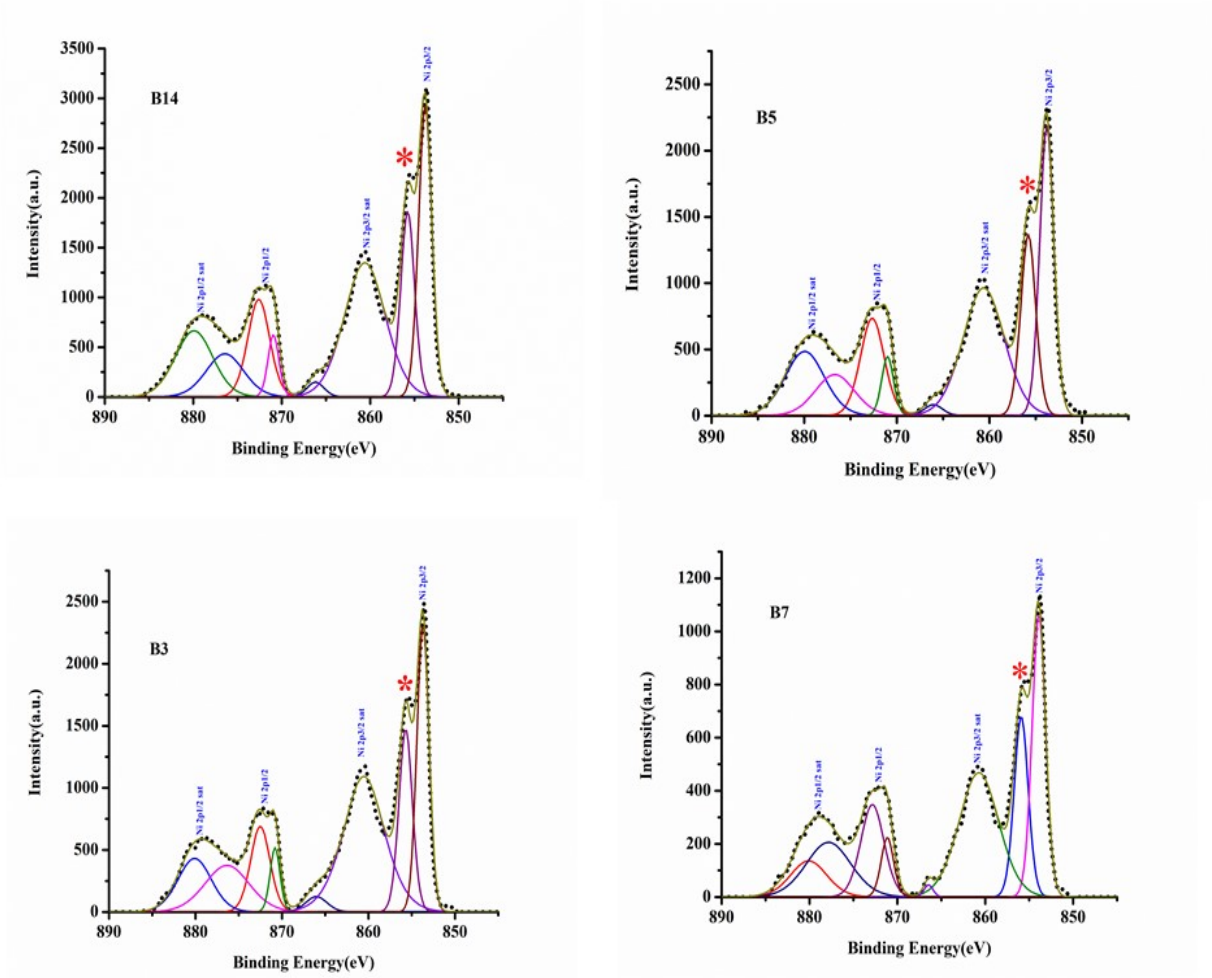

Figure 2.4: High resolution spectra of Ni 2p of different sized NiO NPs: B14: 8.27 nm, B5: 15.67 nm, B3: 27.6 nm and B7: 47.6 nm.

Table 2.2 shows the binding energy difference between Ni 2p3/2 and Ni 2p1/2 is ~18 eV which is persistent, while the particles' size had been changed from ~8 nm to ~47 nm. Theoretically, the separation binding energy between these two subshells is ~17 eV, which is almost similar to the measures value, like ~18 eV. Due to the spin-orbit multiple splitting is consistent while the particles' size changes. Therefore, it is reasonable to say that the oxidation state of Ni ion is 2+ consistent for all samples.

Table2.2: XPS binding energy of Ni 2p regions, including 2p3/2, 2p1/2 and satellite peaks

Samples	Particles Size(nm)	2p3/2	2p3/2 sat	2p1/2	2p1/2 sat	Shoulder Peak (*)	Δ=(2p1/2-2p3/2)
B14	8.27	853.8	860.6	871.9	879.2	855.7	18.1
B5	15.67	853.8	860.6	872	879.3	855.6	18.2
B3	27.60	853.7	860.5	871.9	879.3	855.7	18.2
B7	47.60	853.9	860.7	872.0	879.1	855.7	18.1

Previous work has reported on the presence of secondary satellite peak (*) in the higher energy side for NiO nanoparticles [8],[7]. The secondary satellite peak is attributed predominantly to non-local screening at the surface of the nanoparticles. In the arrangement of the NiO atoms, one nickel atom is surrounded by six oxygen atoms. Since a NiO_6 unit usually is created in the structure of the NiO atomic ordering, local and non-local screening occurs at the surface of the nanoparticles. The creation of a hole by XPS in the Ni 2p level strongly interacts with the hole at the Ni 3d levels. This Coulomb repulsion force is minimized by an incoming electron from the 3d levels, which are hybridized with the O 2p levels from the neighboring O in the NiO6 unit. This leads to local screening effects. If the hole-to-hole interaction occurs between the Ni and near-neighbor O's in larger clusters, then it is referred to as non-local screening, As the oxidation state of nickel ion and chemical environment of NiO remains similar with the changing particles' size, the satellite peak appears at a fixed higher binding energy side of Ni 2p3/2. Biju and Khadar [7] reported that the satellite peak was at 1.5 eV higher binding energy side of Ni 2p3/2. For my samples, the XPS high-resolution spectra show that the satellite peak consistently occurs at ~1.88 eV higher binding energy in relation to the Ni 2p3/2 peak. A

variation in the intensity of the satellite peak with NP size is found to occur for my samples. Due to the surface to volume ratio, a greater amount of local and non-local screening is expected to occur on the surface of the smaller particles and vice versa. Figure 2.5 and fitting analyses show that the intensity of satellite peak increases with the increase of the size of the nanoparticles. However, this is in contrast to the hypothesis put forward by Biju and Khadar [7].

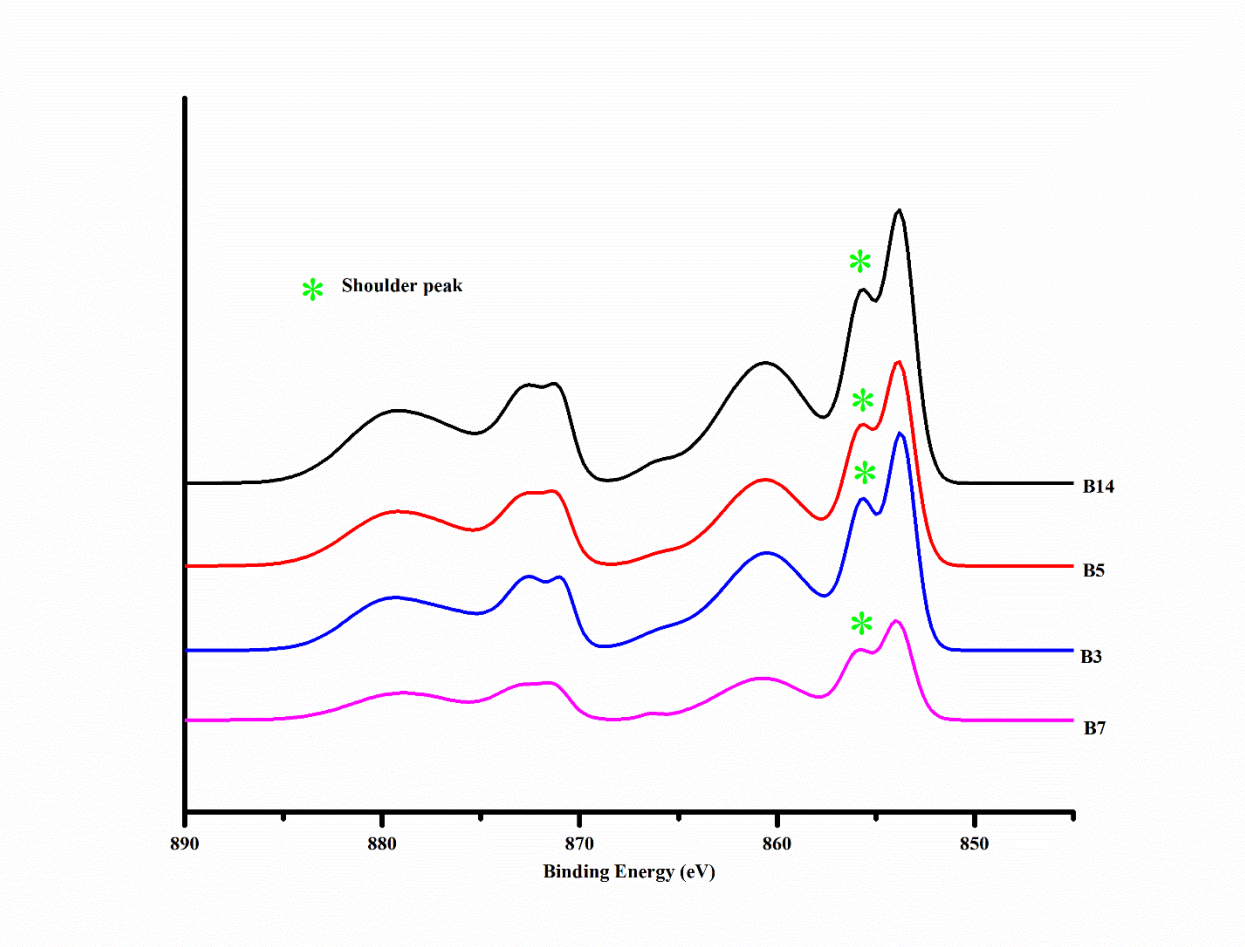

Figure 2.5: Ni2p XPS fitted data of different sized nanoparticles. The size of particles at sample B14, B5, B3, and B7 is 8.27 nm, 15.67 nm, 27.6 nm, and 47.6 nm respectively.

Therefore, there must be a separate, or alternate, mechanism responsible for the satellite peak broadening than the one put forward by these authors. It may be possible that the upper (near the top of the valence band) energy band characteristics associated with the shake-up process responsible for the satellite peak vary with NP size, for the size range of my study, so as

to affect the broadening of the peak. Ab initio calculations may be able to resolve whether this is the case.

Depending on the synthesis process and environment, the surface and the morphology can vary for each batch of NPs. The reported NiO nanoparticles in this manuscript were produced using a thermal decomposition method and two parameters were varied: temperature and decomposition time. In the thermal decomposition method, water was used and the samples were exposed to the ambient environment upon synthesis. Therefore, hydroxylation is a very ubiquitous phenomenon on the surface of NiO nanoparticles. Figure 2.6 shows that all four samples have two impurity peaks (Ni-OH and H_2O) in the O 1s region. Previous studies have

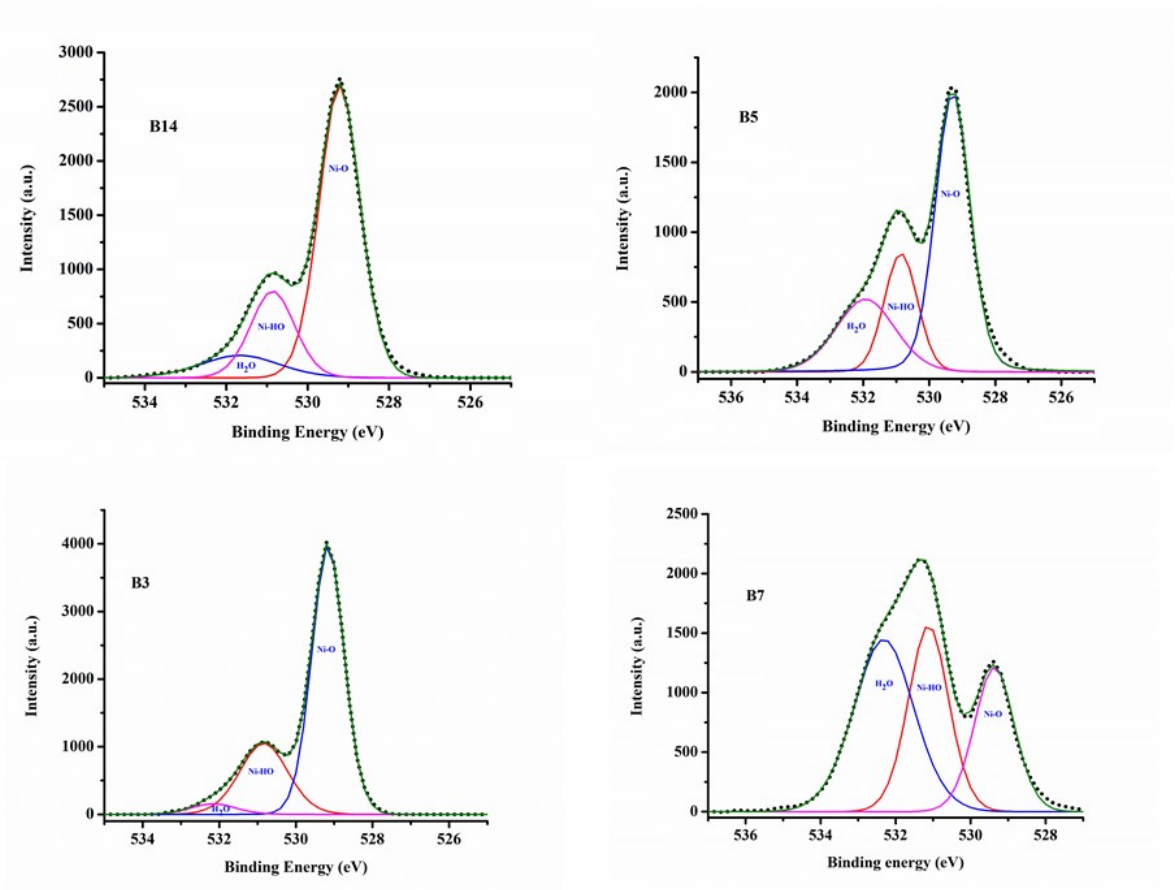

Figure 2.6: The high-resolution O 1s region of B14 (8.27 nm), B5 (15.67 nm), B3 (27.6 nm), and B7 (47.6 nm).

shown that the Ni-OH peak appears at 531.6eV and Ni-H_2O peak at 533.4 eV [8,9] . Our high-resolution O 1s spectra do not show any consistent trend: The spectra for the largest sized NiO NPs, sample B7, are found to have the greatest amount of OH and H_2O species adsorbed on the surface of these particles. Figure 2.7 shows the O 1s peaks for all of the NiO NP samples. The binding energies for Ni bonded O 1s, OH bonded Ni, and water molecule peaks occur at ~ 529.2 eV, ~530.9 eV, and ~ 532 eV respectively, and are consistent for the different sized NPs. However, the peak broadening was found to vary among the different NP samples.

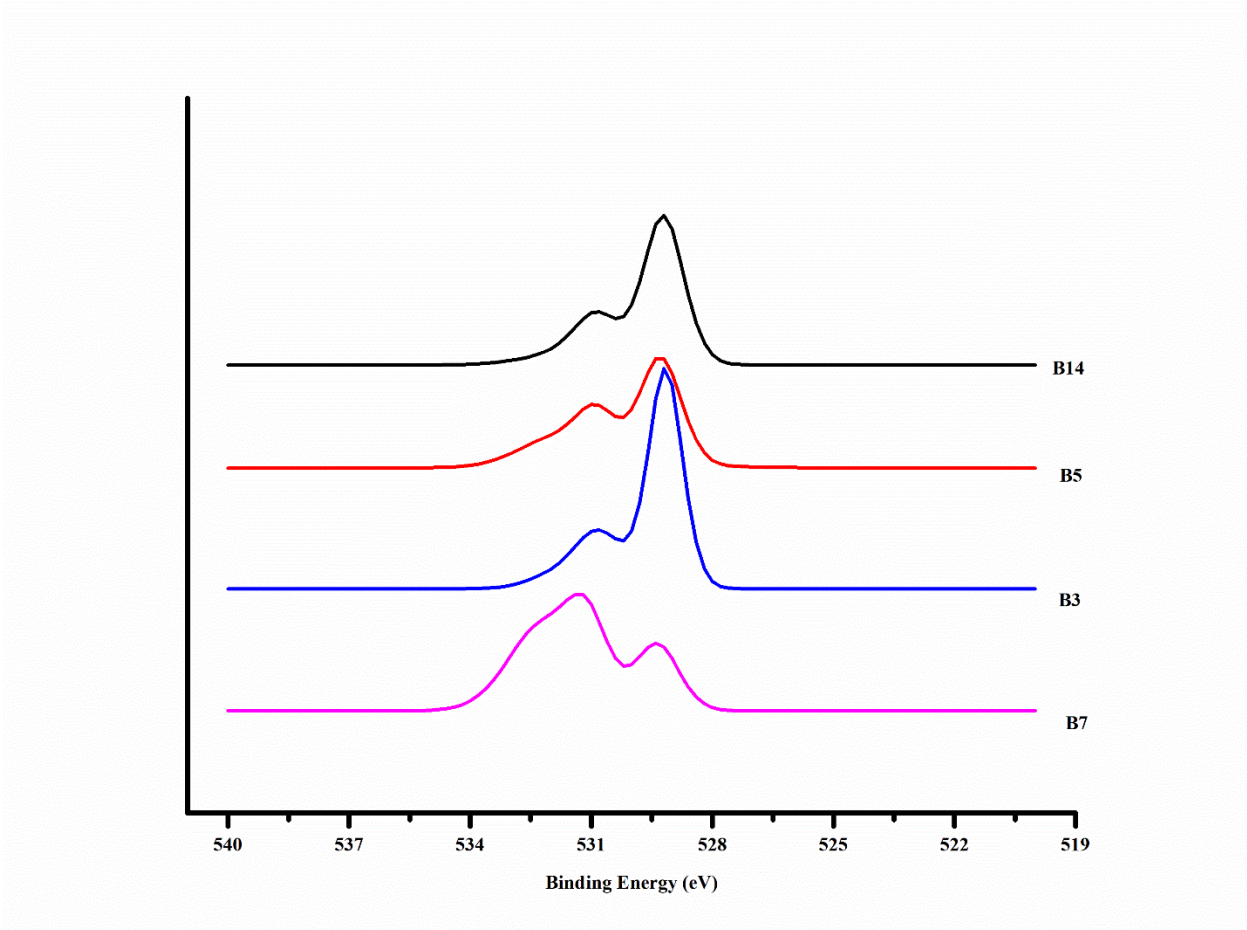

Figure 2.7: XPS data of O 1s region for B14 (8.27 nm), B5 (15.67 nm), B3 (27.6 nm), and B7 (47.6 nm).

As was noted above, the synthesis process and the exposure to the ambient environment can both affect the surface contamination of nanoparticles. For the various samples studied here,

it is clear that the surface OH and H2O content for NP samples B3, B5 and B14 is relatively consistent. However, the surface OH and H2O content for B7 NiO NP sample is clearly much larger than that of any other batch of NPs of this study.

Conclusions

NiO nanoparticles of various sizes were successfully synthesized using the thermal decomposition method. The different sized NiO nanoparticles, varying in size from 8.3 to 47.6 nm, were synthesize by modifying the decomposition time and temperature. XRD analysis was used to interrogate the structural properties of the NiO NPs. The values for the size of the NPs were determined using the Scherrer formula and the XRD patterns. X-ray photoelectron spectroscopy (XPS) was used to investigate the oxidation state of constituent elements and the chemical environment of the NiO nanomaterials. The XPS analyses verified that the binding energy of each peak at Ni 2p region remains constant for all NiO NPs, which is consistent with the +2 oxidation state of Ni. An extra satellite peak occurs on the higher energy side of Ni 2p3/2 peak in the XPS spectra for all of the NiO NP samples. Most importantly, I found that the hypothesis of Biju and Khadar [7], which claims that the intensity of the secondary satellite peak occurring just on the higher energy side of the Ni 2p3/2 peak, is directly affected by the surface-to-volume ratio of NiO NPs and should therefore increase as the NP size decreases, is false. My study shows that just the opposite is true. This will have to be studied further, perhaps using ab initio computational methods, in order to determine the nature of the mechanism responsible for the effect. The O 1s peak is found to have two additional contributions from the contamination of the surface of the NiO NPs by hydroxylation and water molecule adsorption.

References

[1] N. Dharmaraj, P. Prabu, S. Nagarajan, C. H. Kim, J. H. Park, and H. Y. Kim, "Synthesis of nickel oxide nanoparticles using nickel acetate and poly(vinyl acetate) precursor," *Mater. Sci. Eng. B*, vol. 128, no. 1, pp. 111–114, Mar. 2006.

[2] C. Bréchignac, P. Houdy, and M. Lahmani, *Nanomaterials and Nanochemistry*. Springer Science & Business Media, 2008.

[3] M. El-Kemary, N. Nagy, and I. El-Mehasseb, "Nickel oxide nanoparticles: Synthesis and spectral studies of interactions with glucose," *Mater. Sci. Semicond. Process.*, vol. 16, no. 6, pp. 1747–1752, Dec. 2013.

[4] S. Hasan, R. A. Mayanovic, and M. Benamara, "Investigation of novel inverted NiO@Ni $_{x}$ Co $_{1-x}$ O core-shell nanoparticles," *AIP Adv.*, vol. 8, no. 5, p. 056305, May 2018.

[5] S. Hasan, R. A. Mayanovic, and M. Benamara, "Synthesis and Characterization of Novel Inverted NiO@NixMn1-xO Core-Shell Nanoparticles," *MRS Adv.*, vol. 2, no. 56, pp. 3465–3470, 2017.

[6] M. D. Hossain, "Experimental And Theoretical Analyses Of The Structural, Electronic And Magnetic Properties Of Novel Inverted Core-Shell a-CR2O3@a-Mxcr2-Xo3-Y (M=Co, Ni, Mn, Fe) Nanoparticles," p. 106.

[7] V. Biju and M. A. Khadar, "Electronic Structure of Nanostructured Nickel Oxide Using Ni 2p XPS Analysis," p. 7. Received 3 January 2002; accepted in revised form 17 May 2002

[8] M. A. Peck and M. A. Langell, "Comparison of Nanoscaled and Bulk NiO Structural and Environmental Characteristics by XRD, XAFS, and XPS," *Chem. Mater.*, vol. 24, no. 23, pp. 4483–4490, Dec. 2012.

CHAPTER 3: CONCENTRATION-DEPENDENT MAGNETIC PROPERTIES OF NIO@$MN_XNI_{1-X}O$ INVERTED CORE-SHELL NANOPARTICLES

Abstract

Magnetic core shell nanoparticles (CSNs) are promising because of the potential applications in memory, spintronics device, quantum computing, MRI imaging, spin valve, hyperthermia, and other important areas. The magnetic CSNs have two different regions, such as an antiferromagnetic (AFM) component whereas the other component is ferro/ferrimagnetic (FM/FiM). Here, inverted magnetic core shell NPs, NiO (AFM) core and $Ni_xMn_{1-x}O$ shell (FiM) are discussed. The CSNs were synthesized using a two-step process. Firstly, NiO NP's were grown using the thermal decomposition method and secondly Mn was incorporated by way of the hydrothermal epitaxy process in the CSN formation. The magnetic properties of NiO@$Ni_xMn_{1-x}O$ CSNs are directly dependent on the Mn doping concentration. SQUID magnetometry measurements show that higher coercivity (4733 Oe) and exchange bias (1730) were found at a Mn concentration in NiO@$Ni_xMn_{1-x}O$ CSNs attained with a starting $MnCl_2$ aqueous solution having 0.08 M Mn. X-ray diffraction analysis confirms that all of the NiO@$Ni_xMn_{1-x}O$ CSN samples have the rock salt crystal structure. The XPS measurements verify that the oxidation state of Ni (2+) and Mn (2+) are independent of doping concentration of Mn in the CSNs. The size distribution of the particles was calculated from the low resolution TEM image and the HRTEM images confirm the epitaxial growth both of the shell in relation to the core of the NiO@$Mn_xNi_{1-x}O$ CSNs.

Introduction

Magnetic nanoparticles have potential applications in random excess memory, spintronics device, quantum computing, MRI imaging, spin valve, hyperthermia, and other crucial areas [1]–[3]. Magnetic core-shell nanoparticles (CSNs) are very promising multifunctional nanoparticles which have very surprising properties at the interface of two different magnetic phases. The magnetic core shell nanoparticles provide the flexibility to switch core and shell phases and, thereby, to create novel inverted magnetic core shell nanoparticles, in which the core is the antiferromagnetic (AFM) and the shell is the ferro/ferrimagnetic (FM/FiM). The interaction between the core and shell in inverted CSNs exhibits very important magnetic properties that has attracted considerable interest. Among the most notable is the exchange coupling interaction, which may ultimately make these CSNs ideal for nanodevice fabrication.

The properties of magnetic core-shell nanoparticles can be modified to tailor them for specific applications. This can be accomplished by using different synthesis processes, varying synthesis parameters, such as pH, temperature, time duration, etc., and by changing the amount or type of dopant in either the core or shell. The synthesis processes have a direct impact on the characteristics of CSNs because these can control the surface, interface, and morphology of the nanoparticles. The hydrothermal method has been used in our laboratory to grow faced and pseudospherical CSNs which in some cases have been found to exhibit substantial exchange bias and coercivity .Other synthesis processes that are frequently used in for preparation of magnetic CSNs are sol-gel, homogenous precipitation, co-precipitation, sono-chemical, micro-emulsion, and impregnation [1], [4], [5]. The doping/substitutional element can also play a key role in dictating the characteristics of the bi-magnetic CSNs. Substitution of 3d transition ions (M), such

as Ni^{2+}, Co^{2+}, Fe^{2+}, Mn^{2+} and Fe^{3+}, in Cr_2O_3 and NiO shell phases has shown to produce wide variability in the strength and nature of the magnetic properties of bi-magnetic $Cr_2O_3@M_xCr_{2-x}O_3$ and $NiO@M_xNi_{1-x}O$ CSNs [5]. These studies suggested that aside from directly impacting the magnetic spin-spin interaction, the substitutional M element concentration may also affect the properties of the interface and potentially the surface regions. However, this has been not completely resolved.

The interface of bi-magnetic CSNs has a significant role in developing the interaction between core and shell by way of the so called exchange bias coupling of CSNs. Meiklejohn and Bean first studied the exchange bias effect in 1956, followed by Jacobs in 1966 [6], [7]. They observed the field cooled (FC) hysteresis loop shifted along the horizontal (applied field) axis with respect to zero field cooled (ZFC) hysteresis loop; in some case, a vertical shift of the FC vs ZFC hysteresis curve along the vertical (magnetization) axis is observed. The exchange bias field is established at the interface of either thin films or core vs shell of CSNs from the interaction between the neighboring magnetic spins in the respective FM/FiM and AFM phases joined at the interface. For the sake of discussion, I will consider only the AFM-FM case. In case of inverted magnetic CSNs, the AFM core spins couple with and cause pinning of the FM spins in the shell directly at the interface and impose a torque on the FM spins in the shell which has to be overcome by the applied magnetic field upon field orientation reversal (i.e., during the hysteresis loop measurement). Provided that the AFM anisotropy is strong enough, the FC vs ZFC hysteresis data will exhibit a significant shift along the field axis, i.e., a significant exchange bias [7]. Aside from the physical manifestations of the bi-magnetic CSNs (e.g., types of phases, degree of crystallinity, morphology, nature of core-shell interface, etc.), the exchange bias and coercivity also depend upon temperature, specifically whether the measurements are made below

or above the Neel temperature, TN, for the AFM phase, and the Curie temperature (Tc) that dictates order vs disorder for the FM or FiM phase. Zeng et. al. reported that the magnetization, coercivity and exchange bias are controlled by geometrical parameters and the chemical composition of the CSNs [8]. It can be assumed that the interface, core-shell ratio, and surface to volume ratio change with the doping concentration. As a result, the total magnetization, coercivity, and exchange bias depend on the doping concentration.

In their initial development of $NiO@M_xMn_{1-x}O$ CSNs, Hassan et al. [1] discovered that $NiO@Mn_xNi_{1-x}O$ CSNs exhibit substantial coercivity (Hc) and exchange bias field (Heb) effects. However, this work was made on $NiO@Mn_xNi_{1-x}O$ CSNs having only one Mn concentration value. In my research, I have synthesized and characterized a series of $NiO@Mn_xNi_{1-x}O$ CSNs having variable Mn concentrations, in order to study the effect of Mn substitution on their magnetic and structural properties. For this, I adopted the same synthesis process that was fist initiated by Hassan et.al [1]. The structural properties were studied using X-ray diffraction (XRD), whereas TOPAS software was used for the Rietveld refinement and size determination of the nanoparticles was determined using the Scherrer equation. Additional structural results were obtained using high-resolution transmission electron microscopy (TEM). The oxidation state for Ni and Mn, along with the chemical environment characteristics, were determined using X-ray photoelectron spectroscopy. The magnetic hysteresis loop and temperature-dependent magnetization data were measured from the CSNs using SQUID magnetometry.

Experimental Methods

Nickel oxide nanoparticles were synthesize using thermal decomposition as reported by El-Kemary et. al. [9]. The materials used for this synthesis process include nickel chloride

hexahydrate (0.111 M), sodium hydroxide, hydrazine monohydrate, and ethanol. The thermal decomposition process was made using the following steps: Nickel chloride hexahydrate ($NiCl_2.6H_2O$) was added to ethanol to make a solution and then mN_2H_4 was poured into solution to initiate the initial chemical reaction. NaOH was used to adjust the pH of the solution. Thereafter, a magnetic stirrer was used to stir the solution at room temperature and kept for sufficient time to obtain the participated precursor. The solution was then centrifuged 4-5 times to separate the impurity elements from the precursor. The final product that was obtained is $Ni(OH)_2.0.5H_2O$, which was kept inside an enclosed box at 50ºC for drying. El-Kemary et. al. reported that the final product after drying should be $Ni(OH)_2$. However, XRD measurements of my final product upon drying confirmed that it was Ni (metallic) nanoparticles. The Ni nanoparticles were heated at _50ºC in a box furnace in an oxygen atmosphere for thermal decomposition, thus producing NiO nanoparticles.

A quantity of 0.33g of NiO NPs were added to measured quantities of $MnCl_2$ to produce $NiO@Ni_xMn_{1-x}O$ CSNs using the hydrothermal technique at 200º C for 19 hours. The hydrothermal epitaxy method is a very straightforward synthesis process. HPHCL water was first measured out in a beaker and purged for O_2 using N_2 gas at 50º C. Subsequently, $MnCl_2$ was added to the purged water and sonicated to dissolve the $MnCl_2$ into the water, whereupon the pH was adjusted with HCl. After that, NiO nanoparticles were added to the $MnCl_2$ solution and sonicated for a longer time to dis-agglomerate the NPs in the solution. The solution was next inserted into an autoclave and sealed very tightly and then put inside a furnace at 200º C for 19 hours. After this, the solution was washed to remove impurities by centrifuging, and then dried at room temperature.

The characterization of the NiO@$Ni_xMn_{1-x}O$ CSNs was made using XRD, XPS, TEM, and SQUID magnetometry. A Bruker D8 Discover instrument (source Cu Kα λ= 1.54184 Å) was used at 40 kV and 40 mA to determine the crystal structure of the NPs before and after doping, and the size of the CSNs was measured using Scherrer equation with the TOPAS software. X-ray photoelectron spectroscopic analysis was made by Versaprobe XPS facility at University of Arkansas which has a monochromated Al Kα beam source and Ar and C-60 cluster ion guns. The chemical shift and oxidation state of the constituent elements were determined by XPS measurement and the raw data was fitted using CasaXPS software. The single particle visualization was performed using cryo-transmission electron microscope (TEM). The TEM sample was prepared by mixing NPs in hexane. Firstly, NPs were added to hexane and then sonicated using probe sonicator. The copper grid was used to prepare the CSN sample. A Quantum Design MPMS/XL SQUID magnetometer was used to measure the magnetic properties of CSNs. The samples were loaded inside a soft gel capsule and thereafter the loaded capsule was placed inside chamber of SQUID magnetometer. The FC and ZFC hysteresis loops were measured in the range of 15000Oe to – 15000Oe at 5K temperature. The magnetization (M) vs temperature (T) was performed at 100 Oe from 5K to 300K.

Results and discussion

The shell and core region of the CSNs have similar crystalline structure. Figure 3.1 shows XRD data of concentration-dependent NiO@$Ni_xMn_{1-x}O$ CSNs at room temperature. I will use the Mn_no. of M_NiO abbreviation, where no. of M stands for the number of moles of MnCl2 used in the preparation of the CSNs, for the concentration-dependent NiO@$Ni_xMn_{1-x}O$ CSNs designations.

All four samples exhibit very similar XRD patterns. Irrespective of the Mn concentration, as controlled using the initial concentration of the MnCl2 solution used for the shell formation procedure in the range from 0.065 M to 0.1M, has not changed the position (in two-theta) of the individual peaks indicative of the rock-salt structure. Furthermore, I do not observe any additional impurity peaks in the XRD data. The tuning of manganese to NiO nanoparticles in

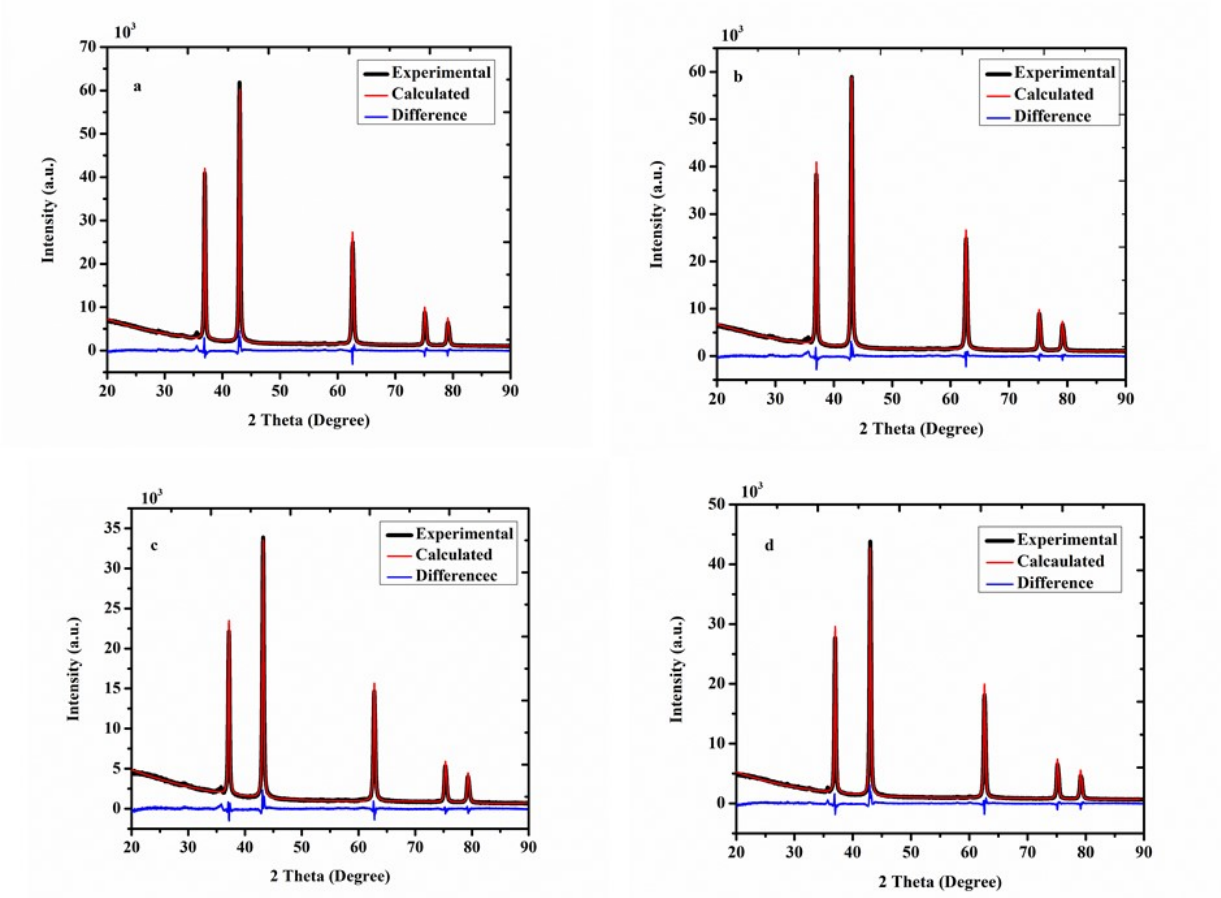

Figure 3.1: X-ray diffraction data of (a) Mn_0.065 M_NiO (b) Mn_0.08 M_NiO (c) Mn_0.009 M NiO (d) Mn_0.1 M NiO.

different concentration did not change the crystal structure of the samples. NiO nanoparticles and NiO@$Ni_xMn_{1-x}O$ CSNs have same rock salt crystal structures with Fm3m symmetry. The raw XRD data was analyzed with help of very powerful TOPAS software.

The Scherrer equation has been used to calculate the size of the nanoparticles. Table 3.1 shows the results from the fitting of the XRD data and use of the Scherrer equation to determine the size of the NiO NPs and the NiO@$Ni_xMn_{1-x}O$ CSNs. The comparison between NiO NPs size and corresponding NiO@$Ni_xMn_{1-x}O$ size provides a very clear visualization of the shell formation surrounding the NiO core. High-resolution TEM analysis can be utilized to augment the size determination of the core vs the shell in CSNs.

Table 3.1: Comparison the size of NiO NPs and Mn doped NiO CSNs.

Sample Level	CNP (NiO@NixMn1-xO) Particle Diameter (nm)	NiO NP size (nm)	Moles of Mn in Aq. Solution
NiO@$Ni_xMn_{1-x}O$_1	32.22	30.6	0.065
NiO@$Ni_xMn_{1-x}O$_2	29.70	27.5	0.080
NiO@$Ni_xMn_{1-x}O$_3	27.85	27.5	0.090
NiO@$Ni_xMn_{1-x}O$_4	30.80	30.6	0.100

In our research, we aimed to compare the magnetic properties of four different CSNs samples. The samples were differentiated by the amount of Mn incorporation in the shell of the CSNs. Figure 3.2 shows the ZFC and FC hysteresis loops for each of the Mn incorporated CSN samples. It is evident from the figure that Mn-NiO CSNs shows substantial coercivity in the hysteresis loop curves and an exchange bias shift, depending upon the Mn concentration. The coercivity varies from ~659 Oe to ~ 4587.5 Oe depending on the amount of Mn incorporation. It should be noted that the NiO core size is essentially the same for all the samples but the Mn concentration is different for each of the samples. The highest coercivity, 4587.5 Oe, was found

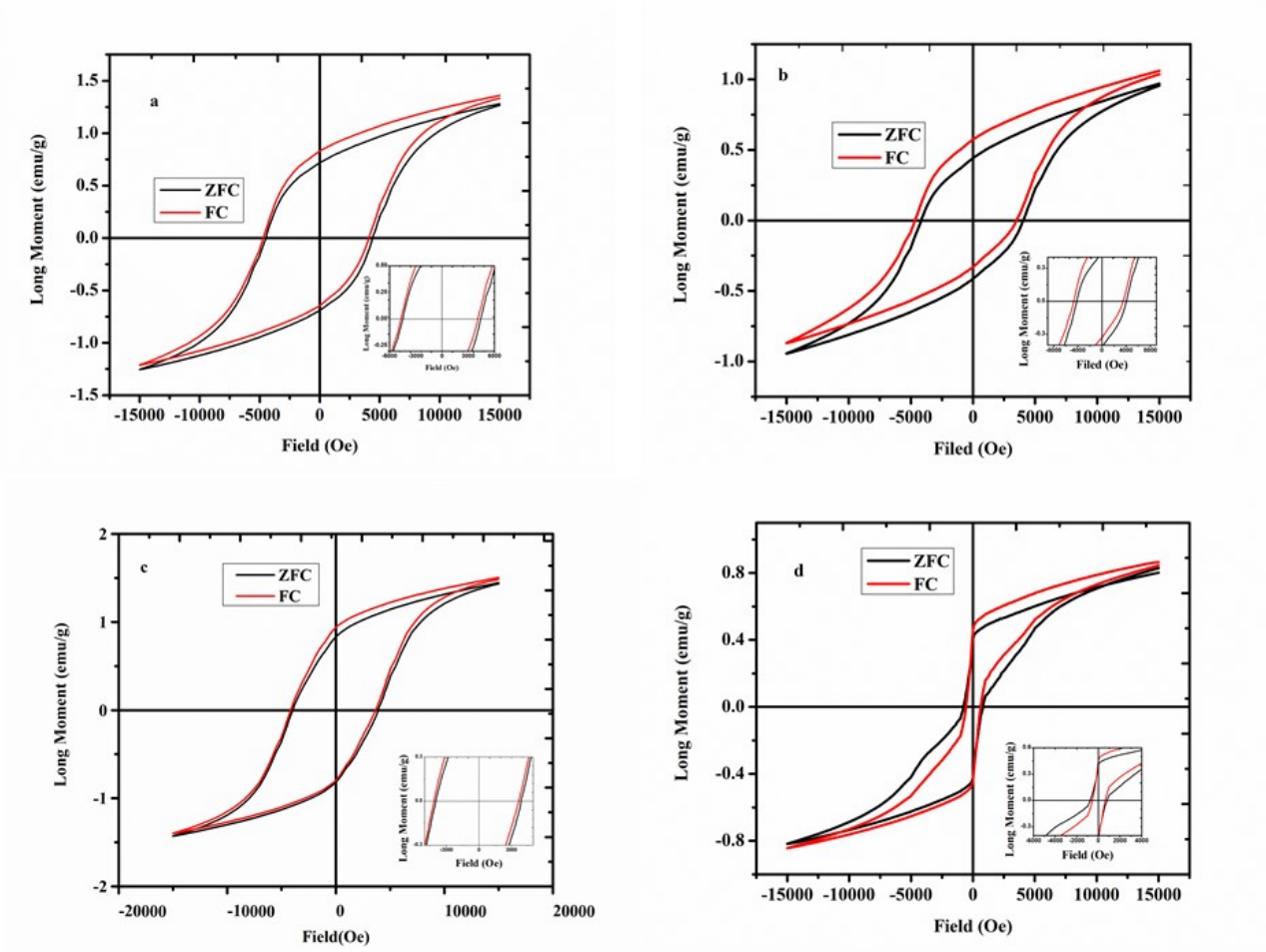

Figure 3.2: Zero field cooled (ZFC) and field cooled (FC) hysteresis loop measurement data for the NiO@$Ni_xMn_{1-x}O$ CSNs samples: (a) Mn_0.065M_NiO (b) Mn_0.08M_NiO (c) Mn_0.09M_NiO and (d) Mn_0.1M_NiO.

for 0.08 M CSN sample and the lowest coercivity, 659 Oe, occurs for the 0.1 M CSN sample Figure 3.2 shows a shift of FC hysteresis loop in the negative H axis and a vertical shift along the M axis. The maximum exchange bias field of 1730 Oe is found for the 0.08 M CSN sample and the minimum exchange bias field of 201 Oe was found for the 0.09 M CSN sample. The calculation of exchange bias was made using $Heb= ((H_{ZFC+} -H_{FC+}) + (H_{FC-} - H_{ZFC-}))/2$ formula [1], [10]. The results for the coercivity and the exchange bias field values are summarized for all of the samples in Table 3.2.

Table 3.2: Coercivity (Hc) and exchange bias field (Heb) of the Mn concentration dependent $NiO@Ni_xMn_{1-x}O$ magnetic CSNs.

Doping concentration of Mn(M)	Coercivity (Oe)	Exchange Bias (Oe)
0.05	450	159
0.065	4587.4	271
0.08	4733	1730
0.09	4067.7	201
0.10	659	203

Figure 3.3 shows that the coercivity vs Mn concentration (as reported using the concentration of the starting $MnCl_2$ solution) in my CSN samples: Here I use a spline connection between points purely for visualization purposes.The maximum in the coercivity is between 0.65 and 0.08 M Mn and most likely closer to

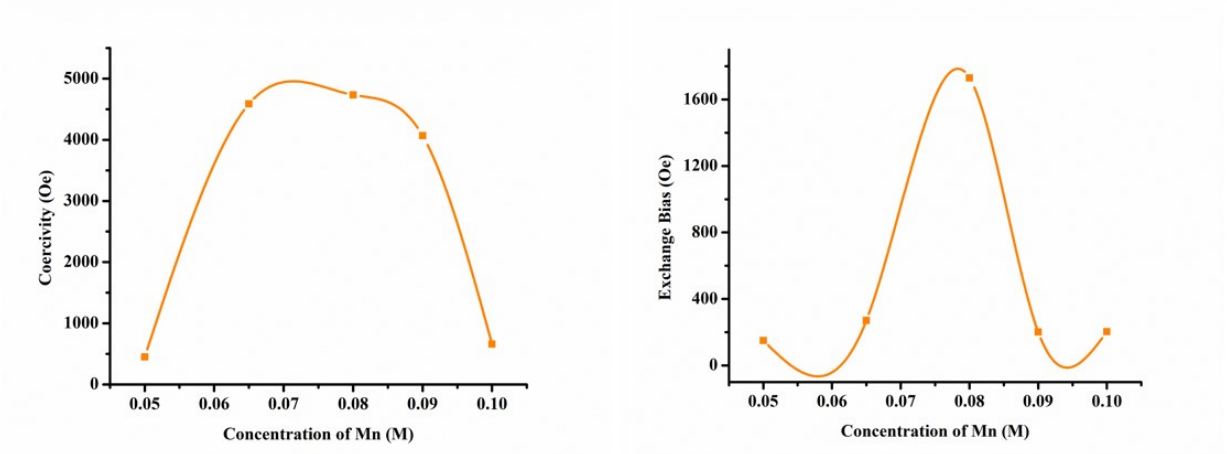

Figure 3.3: The coercivity (Hc) (left) and the exchange bias field (Heb) (right) vs Mn concentration for the samples of the study and from the Hossain et al. (2) study for the 0.8 M Mn sample

the latter value; both below and above this concentration range, the coercivity decreases substantially with Mn content. There may be two mechanisms that contribute to this effect: 1) a percolation spin-occupation effect, and, 2) a Mn-concentration domain size dependent effect. The percolation spin-occupation effect arises from the substitution of Mn spins on the Ni spin lattice.

Hossain et al. [2] showed from initial DFT based calculations that the lowest energy state is one for which the Mn spin maintains the same orientation as the surrounding Ni spins in the spin-ordered (111) planes in the rock-salt $Ni_xMn_{1-x}O$ structure. This gives rise to FiM ordering. As more and more Mn substitute for Ni spins, a critical percolation point is reached for the net FiM moment beyond which an excess of Mn spins are incorporated effectively countering one another, thus reducing the overall magnetic moment. Additionally, excessive incorporation of Mn spins may induce a reduction in the size of the magnetic domains in the shell region. Each of the domains has an overall magnetic dipole moment and the tendency the minimization of energy is in the reduction (i.e. misalignment) the total magnetic moment of each CSN.

Similarly, the exchange bias field (1730 Oe) is also the highest for the 0.08 M Mn concentration CSN sample, showing that the effects for the coercivity and the exchange bias may be linked. In this case, the exchange bias magnetic property arises from the interaction between AFM Ni spins in the core and FiM Ni and Mn spins in the ($Ni_xMn_{1-x}O$) shell. The percolation effect is expected to play a major role in dictating the strength of Heb, just as in the case of the magnetic coercivity.

Figure 3.4 shows the FC and ZFC magnetization curves measured at 5K from the $NiO@Ni_xMn_{1-x}O$ CSNs samples. Each of the samples show individual blocking and Neel temperatures, as shown from the magnetization vs temperature data. Li et al showed that

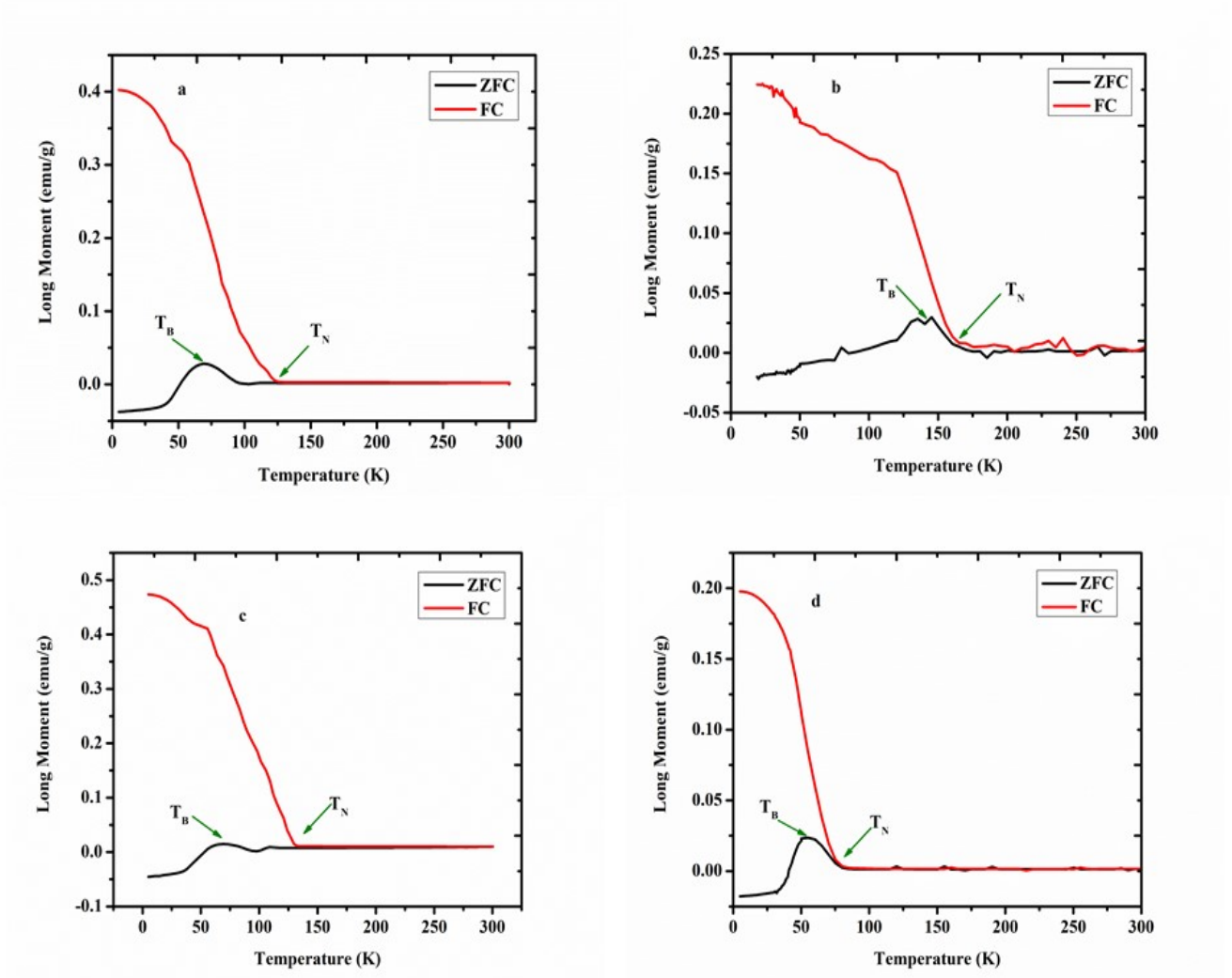

Figure 3.4: Magnetization (M) versus temperature (T) curve measured in the FC and ZFC conditions for $NiO@Ni_xMn_{1-x}O$ CSNs: (a) 0.065 M manganese (b) 0.08 M manganese (c) 0.09 M manganese (d) 0.1 Manganese.

negative magnetization in the ZFC curves can be induced from the competition among the different interactions and tuned with the transition metal content in doped compounds [11]. The

values for the Neel and blocking temperatures are tabulated in Table 3.3 for the samples of study. Both the blocking and Neel temperatures are directly dependent upon Mn content in the CSNs.

The blocking and Neel temperature values are the highest for the 0.08 M Mn concentration CSNs, which is consistent with the other magnetic properties measured from the samples.

Table 3.3: Blocking and Neel temperature of Mn concentration dependent samples.

Mn Concentration (M)	Neel Temperature (T_N)	Blocking Temperature (T_B)
0.065	125	70
0.08	166	140
0.09	132	71
0.1	80	55

Transmission electron microscopy (TEM) provides a clear visualization of the particle's morphology whereas high resolution TEM images provide the opportunity to study the core, shell, and their interface region. Figure 3.5 (a) shows that most of the particles, as is true in the case of all of the CSN samples, are faceted and some of the particles are pseudo spherical. The size of the CSN particles varies from sample to sample, perhaps due to the difference in Mn doping concentration.

Table 3.4 shows the size of the CSNs and the shell thickness, which were calculated from TEM images using imageJ software. The particle size calculated from TEM image is quite a bit different from XRD measured particles size. The discrepancy could be due to an insufficient number of un-agglomerated nanoparticles in the TEM sample for proper statistical analysis. The HRTEM image shown in Figure 3.5 (c) shows the three distinct regions of an individual CSNs including core, shell, and the interface region between them. The HRTEM provides evidence of defects, such as vacancies and misfit dislocations, in the interface and on the surface of a CSN. The thickness of the shell region can be measured directly from the HRTEM images of the CSNs. . Figure 3.5 (d) and (e) show the direction of plane both in core and shell, and FFT also have generated the planes orientation in both two regions (0.065M). The indication of continuity of crystal planes both at core and shell is visible from the FFT image. The interruption of the plane can only be seen at the interface region. Our investigation verified that with the increase in Mn content, both the coercivity and exchange bias decrease. The HRTEM images for the 0.1 M Mn doped CSNs show that these have rougher and thicker interface regions between the core

Table 3.4: Size of the four different NiO@$Ni_xMn_{1-x}O$ CSNs and shell thickness as determined from the TEM image and Scherrer equation.

Concentration of Mn In NiO (M)	Size of CNPs from TEM image (nm)	Size of CNPs using Scherer equation (nm)	Thickness of shell from TEM image (nm)
0.065	26.10	32.20	2.7
0.08	20.78	29.70	2.4
0.09	37.50	27.85	3.4
0.10	33.80	30.80	3.7

and shell. This, in addition to the effect described above, could affect (reduce) the magnetic properties of these particular core shell nanoparticles.

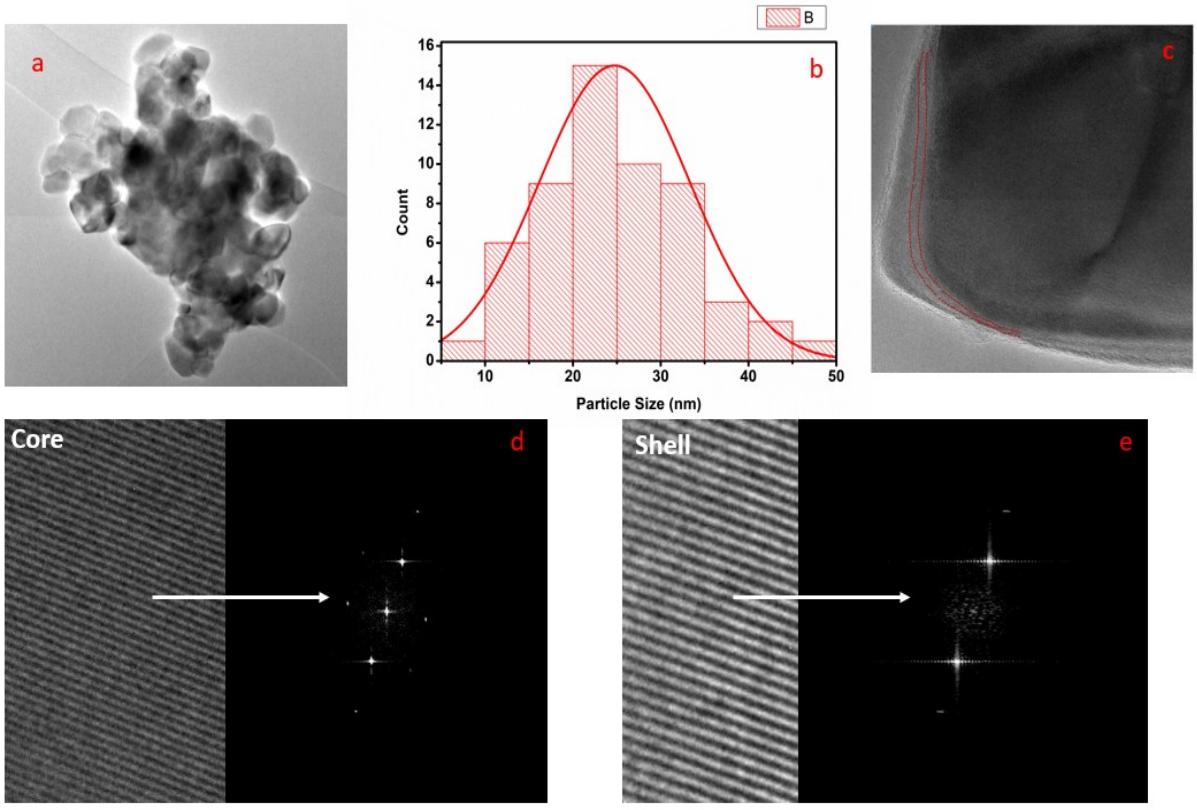

Figure 3.5: (a) Low resolution TEM image of NiO@NixMn1-xO to estimate size distribution and morphology (b) Histogram and normal curve fit of the size distribution of CSNs (c) HRTEM image of core shell region with noticeable interface region (d) Plane orientation and FFT of core (e) Plane direction and FFT of the shell region.

X-ray photoelectron spectroscopy analysis provides the information regarding elemental composition, oxidation state, and chemical shift of the constituent elements. The XPS survey scan of the NiO@$Ni_xMn_{1-x}O$ shows O 1s, Ni2p, Mn2p, C1s peaks, and their corresponding satellite and auger peaks.

The atomic weight percent of Mn is challenging to determine from the high resolution XPS Mn 2p spectra as outlined below . Because the energy positions of the Mn 2p and the Ni auger superimpose, and the Ni auger peak is dominant, it is very difficult to de-convolute one from the other. This problem was resolved by taking the of area of Ni auger peak region from survey scan of NiO. The crystal structure of NiO and $Mn_xNi_{1-x}O$ is similar, as consequence the positions of Ni2p 3/2 and Ni 2p1/2 have the same binding energy for both. The secondary satellite peak at ~1.8 eV higher binding energy side of the Ni2p 3/2 appears to be slightly different before and after substitution of manganese.

Figure 3.6 shows that the Ni 2p3/2 region of the NiO NPs has a very prominent and distinct shoulder (i.e., satellite) peak (*). Conversely, the Ni2p 3/2 region of $NiO@Ni_xMn_{1-x}O$ (0.08 M) CSN peak has a less distinct shoulder peak. The intensity of shoulder peak at Ni2p3/2 region is found to be reduced with at higher Mn concentration in $NiO@Ni_xMn_{1-x}O$ CSNs. The

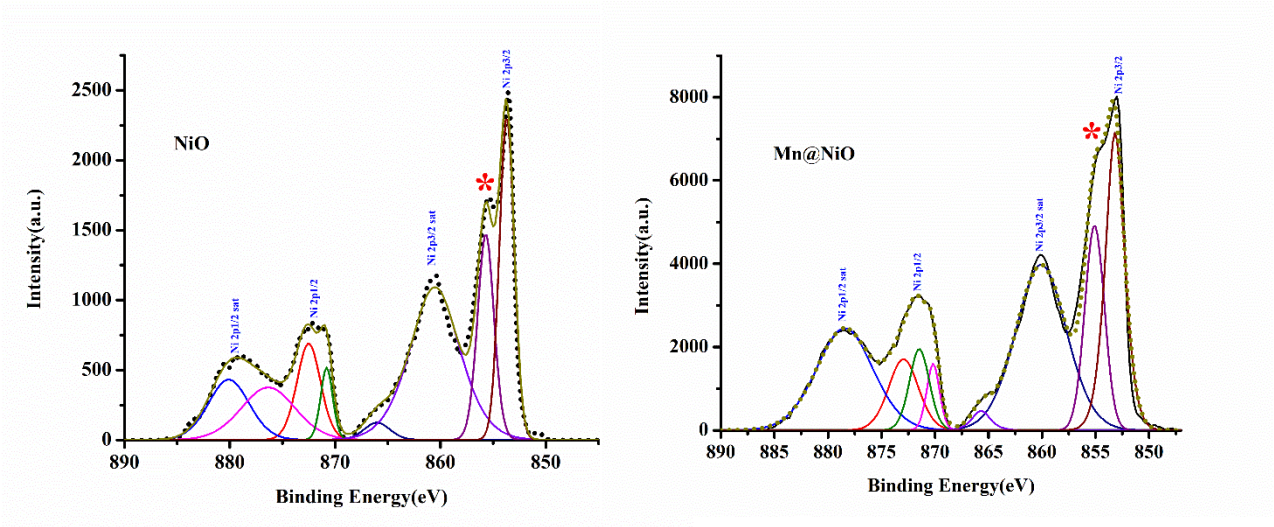

Figure 3.6: High resolution spectra of Ni 2p of NiO and $NiO@Ni_xMn_{1-x}O$ (0.08M Mn).

highest Mn doped (0.1M) CSNs shows no satellite peak at all in the high-resolution Ni 2p spectra. This suggests that substitution of Mn has a direct effect on the intensity of the Ni 2p3/2 XPS peak.

The Ni LVV auger peak appears in the high-resolution XPS, Mn 2p3/2 and Mn 2p1/2 peaks, at ~645 eV, measured from the NiO@$Ni_xMn_{1-x}O$ CSNs. Fitting of the overall Mn 2p (2p3/2 and 2p1/2) XPS peaks was attempted based on known peak separation, peak area ratio, peak widths constraints and known binding energy position of the Ni LVV auger peak. Figure 3.7 shows the overall Mn 2p (2p3/2 and 2p1/2) high resolution peak for four different CSN samples. The Mn 2p3/2 peak clearly shows evidence of multiplet splitting effects, as is common

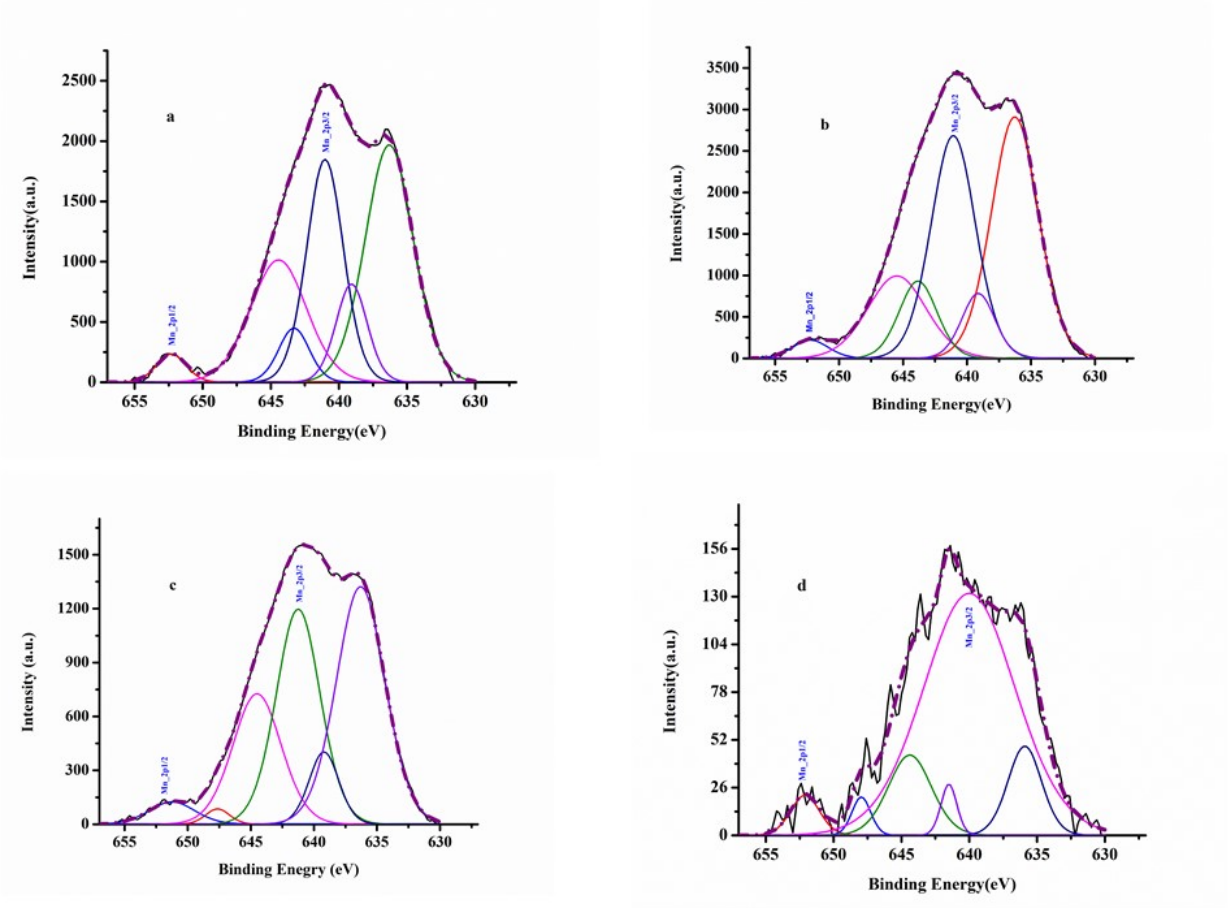

Figure 3.7: The high-resolution XPS Mn 2p peaks of (a) Mn_0.065 M (b) Mn_0.08 M (c) Mn_0.09 M (d) Mn_0.1 M CSN samples.

for a number of compounds containing 3d transition metals. For that reason 3 – 4 peaks are used to fit the overall Mn 2p3/2 features, whereas a peak at ~645 eV is included to account for the Ni LVV auger line. An additional peak, most likely a satellite feature, is included at ~648 eV in the fitting. The predominant higher binding energy Mn 2p3/2 peak is marked in Figure 3.7. The figure clearly shows that the Mn 2p3/2 peak becomes more dominant with increasing Mn concentration. However, quantitative elemental analysis is not possible until the constraints on the area of the Ni LVV auger peak are known.

Conclusions

NiO@$Ni_xMn_{1-x}O$ CSNs were synthesized by following a two-step synthesis procedure. The NiO core was produced using the thermal decomposition method and the $Ni_xMn_{1-x}O$ shell of the CSNs was synthesized using a hydrothermal method. The crystal structure and the size distribution of both the NiO NPs, prior to shell growth, and the CSNs were determined using XRD methods, for which the XRD data were fitted using TOPAS software. The structural analysis verified the samerock-salt crystal structure of the NiO NPs and NiO@$Ni_xMn_{1-x}O$ CSNs, for all Mn concentrations. XPS measurements indicate the oxidation state of Ni and Mn is +2 and that the Mn concentration does not affect the positions of Ni 2p , Mn 2p and O1s peaks. However, a secondary satellite peak occurring just above, in binding energy, the Ni 2p3/2 peak is found to undergo reduction in intensity with increasing Mn concentration in the NiO@$Ni_xMn_{1-x}O$ CSNs. The SQUID magnetometry measurement show that both the coercivity and exchange bias field show non-monotonic maximal behavior as a function of Mn concentration, with the maximum coercivity and exchange bias occurring for 0.08 M Mn content. The size distribution

of the $NiO@Ni_xMn_{1-x}O$ CSNs were calculated from low resolution TEM images and generally agree with the XRD results. The HRTEM images of the CSNs show epitaxial growth of the shell over the core. TheHRTEM images also show defect structure in the interface regions of the CSNs.

References

[1] S. Hasan, R. A. Mayanovic, and M. Benamara, "Synthesis and Characterization of Novel Inverted NiO@NixMn1-xO Core-Shell Nanoparticles," *MRS Adv.*, vol. 2, no. 56, pp. 3465–3470, 2017.

[2] N. J. Borys, M. J. Walter, J. Huang, D. V. Talapin, and J. M. Lupton, "The Role of Particle Morphology in Interfacial Energy Transfer in CdSe/CdS Heterostructure Nanocrystals," *Science*, vol. 330, no. 6009, pp. 1371–1374, Dec. 2010.

[3] M. D. Hossain, R. A. Mayanovic, R. Sakidja, and M. Benamara, "An experimental and theoretical study of the optical, electronic, and magnetic properties of novel inverted α-Cr2O3@α-Mn0.35Cr1.65O2.94 core shell nanoparticles," *J. Mater. Res.*, vol. 32, no. 02, pp. 269–278, Jan. 2017.

[4] S. Hasan, R. A. Mayanovic, and M. Benamara, "Investigation of novel inverted $NiO@Ni_xCo_{1-x}O$ core-shell nanoparticles," *AIP Adv.*, vol. 8, no. 5, p. 056305, May 2018.

[5] M. D. Hossain, R. A. Mayanovic, R. Sakidja, M. Benamara, and R. Wirth, "Magnetic properties of core–shell nanoparticles possessing a novel Fe(II)-chromia phase: an experimental and theoretical approach," *Nanoscale*, vol. 10, no. 4, pp. 2138–2147, 2018.

[6] R. L. Stamps, "Mechanisms for exchange bias," *J. Phys. Appl. Phys.*, vol. 33, no. 23, pp. R247–R268, Dec. 2000.

[7] M. D. Hossain, "Experimental And Theoretical Analyses Of The Structural, Electronic And Magnetic Properties Of Novel Inverted Core-Shell a-CR2O3@a-Mxcr2-Xo3-Y (M=Co, Ni, Mn, Fe) Nanoparticles," p. 106.

[8] H. Zeng, S. Sun, J. Li, Z. L. Wang, and J. P. Liu, "Tailoring magnetic properties of core⁄shell nanoparticles," *Appl. Phys. Lett.*, vol. 85, no. 5, pp. 792–794, Aug. 2004.

[9] M. El-Kemary, N. Nagy, and I. El-Mehasseb, “Nickel oxide nanoparticles: Synthesis and spectral studies of interactions with glucose,” *Mater. Sci. Semicond. Process.*, vol. 16, no. 6, pp. 1747–1752, Dec. 2013.

[10] H. Khurshid, M.-H. Phan, P. Mukherjee, and H. Srikanth, “Tuning exchange bias in Fe/γ-Fe $_2$ O $_3$ core-shell nanoparticles: Impacts of interface and surface spins,” *Appl. Phys. Lett.*, vol. 104, no. 7, p. 072407, Feb. 2014.

[11] C. Li *et al.*, “Negative magnetization and the sign reversal of exchange bias field in Co(Cr $_{1-x}$ Mn $_x$) $_2$ O $_4$ ($0 \leq x \leq 0.6$),” *J. Appl. Phys.*, vol. 123, no. 9, p. 093902, Mar. 2018.

CHAPTER 4: SUMMARY

I have synthesized NiO NPs using the thermal decomposition method, where I varied the decomposition time and temperature to modify the size of the NPs. The purpose of this work was to determine from XPS spectroscopy whether the well-known secondary satellite peak occurring as a shoulder feature of the Ni 2p3/2 feature is directly dependent on the size of NiO NPs. The high-resolution spectra of the Ni 2p region, consisting of the Ni 2p3/2, Ni 2p1/2 and their corresponding satellite peaks, were measured from NiO NPs ranging in size from 8.3 to 47.3 nm. The binding energy positions of the Ni 2p3/2, Ni 2p1/2, and satellite peaks were found to be the same for all NP samples., A distinct secondary satellite peak, occurring at ~1.8 eV higher in binding energy than the main Ni 2p3/2 peak, was observed for all NiO NP samples. The secondary satellite was found to increase in intensity with the increase in size of the NiO NPs. This directly contradicts the conjecture offered by Biju and Khadar [8], suggesting that the intensity of the secondary satellite peak should increase as the NP size decreases due to the increase in the surface-to-volume ratio, and thereby surface defects, with reduced NP size. This suggests that a separate mechanism, other than non-local screening due to defect structure, may be responsible for the secondary satellite peak. In similar fashion, the O 1s peak also showed some variations depending on particular NP sample. The variations in the O 1s peak are attributed to the presence of H_2O and NiOH on the surface of the NPs, the former due to adsorption in air and the latter occurring during the synthesis process.. In my second study, I analyzed predominantly the structural and magnetic properties of NiO@$Ni_xMn_{1-x}O$ CSNs having varying Mn concentrations. The Mn concentration was varied using $MnCl_2$ aqueous solutions

ranging from 0.065 M to 0.1 M during the second step of the CSN synthesis process involving hydrothermal epitaxial growth technique to fabricate the $Ni_xMn_{1-x}O$ shell over the core of the CSNs. X-ray diffraction data showed that the rock-salt structure was preserved after hydrothermal synthesis and CSN formation, for all samples. Furthermore, the fitting of the XRD data and using the Scherrer equation showed the CSNs are in general slightly larger than the NiO NPs, indicating shell formation. High-resultion XPS measurements of the Ni 2p and Mn 2p features show that both Ni and Mn have the +2 oxidation state in the CSNs, irrespective of Mn concentration. SQUID magnetometer measurements of the $NiO@Ni_xMn_{1-x}O$ CSNs show that Hc and Heb exhibit peaked functional behavior with Mn concentration. The maxima for both Hc (4733 Oe) and Heb (1730 Oe) occur for 0.08 M Mn content. HRTEM images and fast Fourier transforms analysis of the images show epitaxial growthof the shell region of $NiO@Ni_xMn_{1-x}O$ CSNs. Furthermore, the HRTEM images show that the CSNs exhibit defects within the core-shell interface, particularly vacancies and misfit dislocations.

References

[1] C. Bréchignac, P. Houdy, and M. Lahmani, *Nanomaterials and Nanochemistry*. Springer Science & Business Media, 2008.

[2] S. Hasan, R. A. Mayanovic, and M. Benamara, "Investigation of novel inverted $NiO@Ni_x Co_{1-x} O$ core-shell nanoparticles," *AIP Adv.*, vol. 8, no. 5, p. 056305, May 2018.

[3] S. Hasan, R. A. Mayanovic, and M. Benamara, "Synthesis and Characterization of Novel Inverted NiO@NixMn1-xO Core-Shell Nanoparticles," *MRS Adv.*, vol. 2, no. 56, pp. 3465–3470, 2017.

[4] A. López-Ortega, M. Estrader, G. Salazar-Alvarez, A. G. Roca, and J. Nogués, "Applications of exchange coupled bi-magnetic hard/soft and soft/hard magnetic core/shell nanoparticles," *Phys. Rep.*, vol. 553, pp. 1–32, Feb. 2015.

[5] N. Dharmaraj, P. Prabu, S. Nagarajan, C. H. Kim, J. H. Park, and H. Y. Kim, "Synthesis of nickel oxide nanoparticles using nickel acetate and poly(vinyl acetate) precursor," *Mater. Sci. Eng. B*, vol. 128, no. 1–3, pp. 111–114, Mar. 2006.

[6] M. Salavati-Niasari, F. Davar, and Z. Fereshteh, "Synthesis of nickel and nickel oxide nanoparticles via heat-treatment of simple octanoate precursor," *J. Alloys Compd.*, vol. 494, no. 1–2, pp. 410–414, Apr. 2010.

[7] M. A. Peck and M. A. Langell, "Comparison of Nanoscaled and Bulk NiO Structural and Environmental Characteristics by XRD, XAFS, and XPS," *Chem. Mater.*, vol. 24, no. 23, pp. 4483–4490, Dec. 2012.

[8] V. Biju and M. A. Khadar, "Electronic Structure of Nanostructured Nickel Oxide Using Ni 2p XPS Analysis," p. 7. Received 3 January 2002; accepted in revised form 17 May 2002

[9] "X-ray photoelectron spectroscopy - Wikipedia." [Online]. Available: https://en.wikipedia.org/wiki/X-ray_photoelectron_spectroscopy. [Accessed: 19-Mar-2019].

[10] R. T. Haasch, "X-Ray Photoelectron Spectroscopy (XPS) and Auger Electron Spectroscopy (AES)," in *Practical Materials Characterization*, M. Sardela, Ed. New York, NY: Springer New York, 2014, pp. 93–132.

[11] "X-ray Photoelectron Spectroscopy (XPS) Reference Pages: Shake Up Structure." [Online]. Available: http://www.xpsfitting.com/2012/08/shake-up-structure.html. [Accessed: 20-Mar-2019].

[12] "[cond-mat/0110222] Shake-up and shake-off excitations with associated electron losses in X-ray studies of proteins." [Online]. Available: https://arxiv.org/abs/cond-mat/0110222. [Accessed: 20-Mar-2019].

[13] K. Byrappa and T. Adschiri, "Hydrothermal technology for nanotechnology," *Prog. Cryst. Growth Charact. Mater.*, vol. 53, no. 2, pp. 117–166, Jun. 2007.

[14] M. D. Hossain, R. A. Mayanovic, R. Sakidja, M. Benamara, and R. Wirth, "Magnetic properties of core–shell nanoparticles possessing a novel Fe(II)-chromia phase: an experimental and theoretical approach," *Nanoscale*, vol. 10, no. 4, pp. 2138–2147, 2018.

[15] N. J. Borys, M. J. Walter, J. Huang, D. V. Talapin, and J. M. Lupton, "The Role of Particle Morphology in Interfacial Energy Transfer in CdSe/CdS Heterostructure Nanocrystals," *Science*, vol. 330, no. 6009, pp. 1371–1374, Dec. 2010.

[16] C. P. Byers *et al.*, "From tunable core-shell nanoparticles to plasmonic drawbridges: Active control of nanoparticle optical properties," *Sci. Adv.*, vol. 1, no. 11, p. e1500988, Dec. 2015.

[17] M. D. Hossain, R. A. Mayanovic, R. Sakidja, and M. Benamara, "An experimental and theoretical study of the optical, electronic, and magnetic properties of novel inverted α-

Cr2O3@α-Mn0.35Cr1.65O2.94 core shell nanoparticles," *J. Mater. Res.*, vol. 32, no. 02, pp. 269–278, Jan. 2017.

[18] "Effect of Cobalt Doping Concentration on the Crystalline Structure and Magnetic Properties of Monodisperse CoxFe3–xO4 Nanoparticles within Nonpolar and Aqueous Solvents - The Journal of Physical Chemistry C (ACS Publications)." [Online]. Available: https://pubs.acs.org/doi/abs/10.1021/jp205088x. [Accessed: 21-Mar-2019].

[19] R. L. Stamps, "Mechanisms for exchange bias," *J. Phys. Appl. Phys.*, vol. 33, no. 23, pp. R247–R268, Dec. 2000.

[20] S. Song, X. Wang, and H. Zhang, "CeO_2-encapsulated noble metal nanocatalysts: enhanced activity and stability for catalytic application," *NPG Asia Mater.*, vol. 7, no. 5, p. e179, May 2015.

[21] H. Ohldag *et al.*, "Correlation between Exchange Bias and Pinned Interfacial Spins," *Phys. Rev. Lett.*, vol. 91, no. 1, p. 017203, Jul. 2003.

[22] K. S. Kumar, V. B. Kumar, and P. Paik, "Recent Advancement in Functional Core-Shell Nanoparticles of Polymers: Synthesis, Physical Properties, and Applications in Medical Biotechnology," *J. Nanoparticles*, vol. 2013, pp. 1–24, 2013.

[23] N. C. Koon, "Calculations of Exchange Bias in Thin Films with Ferromagnetic/Antiferromagnetic Interfaces," *Phys. Rev. Lett.*, vol. 78, no. 25, pp. 4865–4868, Jun. 1997.

[24] M. D. Hossain, "Experimental And Theoretical Analyses Of The Structural, Electronic And Magnetic Properties Of Novel Inverted Core-Shell a-CR2O3@a-Mxcr2-Xo3-Y (M=Co, Ni, Mn, Fe) Nanoparticles," p. 106.

[25] "Graphics Gallery." [Online]. Available: http://magnet.atp.tuwien.ac.at/gallery/exchbias/intuitive.html. [Accessed: 22-Mar-2019].

[26] G. Salazar-Alvarez, J. Sort, S. Suriñach, M. D. Baró, and J. Nogués, "Synthesis and Size-Dependent Exchange Bias in Inverted Core−Shell MnO|Mn_3O_4 Nanoparticles," *J. Am. Chem. Soc.*, vol. 129, no. 29, pp. 9102–9108, Jul. 2007.

[27] M. Mehrmohammadi, K. Y. Yoon, M. Qu, K. P. Johnston, and S. Y. Emelianov, "Enhanced pulsed magneto-motive ultrasound imaging using superparamagnetic nanoclusters," *Nanotechnology*, vol. 22, no. 4, p. 045502, Jan. 2011.

[28] S. E. Inderhees *et al.*, "Manipulating the Magnetic Structure of Co Core/CoO Shell Nanoparticles: Implications for Controlling the Exchange Bias," *Phys. Rev. Lett.*, vol. 101, no. 11, p. 117202, Sep. 2008.

[29] U. Wiedwald and M. Albrecht, Characterization of Nano-particles for magnetic data storage media, Seminar of the Physikalisch-Technische Bundesanstalt, Germany, 2002, February 27